UNIVERSIDAD TECNICA
FEDERICO SANTA MARIA

DEPARTAMENTO
DE INGENIERIA
ELÉCTRICA

Thesis to qualify for the degree of Master of Science in Electrical Engineering

ADMM-Based Long-Horizon Model Predictive Energy Control of Modular Multilevel Converters for High-Power Variable-Speed Drives

Candidate : Sebastián Rivero Albornoz
Thesis Advisor : Dr. Andrés Mora C.
Co-Advisor : Dr. Javier Pereda T.

Valparaíso - Chile
October 12, 2024

Abstract

Multilevel converter topologies have become integral to the technological advancements in power electronics due to their scalability, quality, variety of voltage levels at external ports, fault tolerance, among other features. They play a significant role in meeting the increasing power demands in applications such as HVDC transmission, medium voltage drives, and wind and solar energy conversion. Their wide range of operation brings with it the complex and inherent task of controlling not only external signals but also internal variables, as they are generally composed of passive storage devices like capacitors. Thus, voltage oscillations at certain operating points can significantly affect external performance or damage converter components.

This internal control uses variables inherent to the topology to balance energy between each branch. Therefore, an energy balance control is proposed through the generation of circulating current references without limitation on frequency components, utilizing an arbitrary common mode voltage (CMV) signal while driving an induction motor whose critical operation occurs at low speed with high torque. The control operates at the cluster level, considering their energy model, which includes circulating currents as a degree of freedom and the external currents as a known input, yielding a convex optimization function to solve.

Additionally, with the aim of achieving more optimal and efficient performance, an extended horizon model predictive control is implemented based on an iterative resolution algorithm called Alternating Direction Method of Multiplier (ADMM). Its main feature is solving through the separation of the function to be optimized, with guaranteed convergence given the nature of the model used. Finally, the results are tested through experimental maneuvers on a drive prototype both in steady state and dynamic processes that include low speed and, consequently, greater control demands.

Acknowledgments

Antes que todo, esto va dedicado especialmente a mi abuelo, Modesto, quien desde arriba ve como termino lo que en vida vio como empecé.

Este es el camino que me imaginé recorrer con todas las dificultades de por medio, pero debo añadir que el apoyo y compañía fue más allá de mis expectativas. Partiendo por mi familia, mis padres Marisol y Alfredo, mi abuela Clementina y mi hermana Michelle, agradezco cada gesto, acción y palabra que me entregaron para hacerme saber de lo que soy capaz y que no estoy solo.

Agradezco a mi principal compañera en estos siete años, Gabriela, aquella que me permitió tomar su mano para que este duro trayecto fuera más lindo y ameno gracias a su presencia.

Gracias a todos aquellos compañeros y profesores que tendieron una mano amiga aunque sea una vez e incluso sin intención a ratos, en especial a Cristóbal y Martín con quienes compartí todo el trayecto incluyendo el magíster y a los integrantes del PecLab en la PUC por su gran disposición durante el año que estuve con ellos.

Gracias por las experiencias.

Funding

The work was made possible and supported by FONDECYT Grant 1231030 "Distributed Model Predictive Control for AC/AC Modular Multilevel Converters: Towards Fully Flexible and Fault-Tolerant Topologies" and utilizing the equipment provided by Fondequip Grant EQM210117 "Emulador Flexible PHIL como Plataforma de Investigación para los Desafios de la Transición Energética." and Power & Energy Conversion Laboratory at Pontificia Universidad Católica.

List of Figures

List of Tables

Contents

1. Introduction

For more than a decade, various applications requiring power electronics and their power converters have occupied a significant percentage of the national power grid[4]. Moreover, considering the decarbonization plans that lead to energy production through renewable raw materials without high extraction costs, coupled with the reduction of gas emissions through components that abandon fossil fuels in favor of electric energy.

That said, power converters are the primary means of connecting the needs of each subsystem to the binding conditions of the grid as shown in Fig. 1.1. For example, in the case of photovoltaic (PV) plants [5], where energy must be converted from direct current (DC, =) to alternating current (AC, ∼), or to change the frequency due to turbine rotation as in wind energy conversion processes[6], and even to convert alternating current energy to direct current exclusively for transportation, as in HVDC transmission lines[7]. Thus, power converters are the enabling technology to maximize the use of clean energy directly from variable renewable energy sources accompanied by a reduction in production and operating costs. Therefore, converters are penetrating power grids not only significantly impacting the efficiency, reliability, and energy quality of the different generation, storage and energy consumption technologies, but also influencing the control and operation of the entire power system [8, 9].

In this scenario, modular multilevel cascaded converters (MMCC) emerge as a power converter family suitable for high-power applications [10]. Compared with conventional power converters, the MMCC topologies exhibit several prominent advantages, such as modularity, scalability, power quality, and fault-tolerant operation capability [11, 12, 13, 14] such as stability and power capacity. Among them, the leading exponents for ac to ac power conversion are the back-to-back modular multilevel converter (B2B-M2C), the modular multilevel matrix converter (M3C) and the Hexverter (HxC). These converters can be used for critical ac-ac applications such as low-frequency ac (LFAC) transmission systems, wind power conversion systems (WECS), power system interconnections (60-50 Hz) and medium/high voltage motor drives for pumps, mills, conveyors, marine propulsion, among other applications. Positioning these topologies as the next generation in medium/high voltage and high power applications.[15,

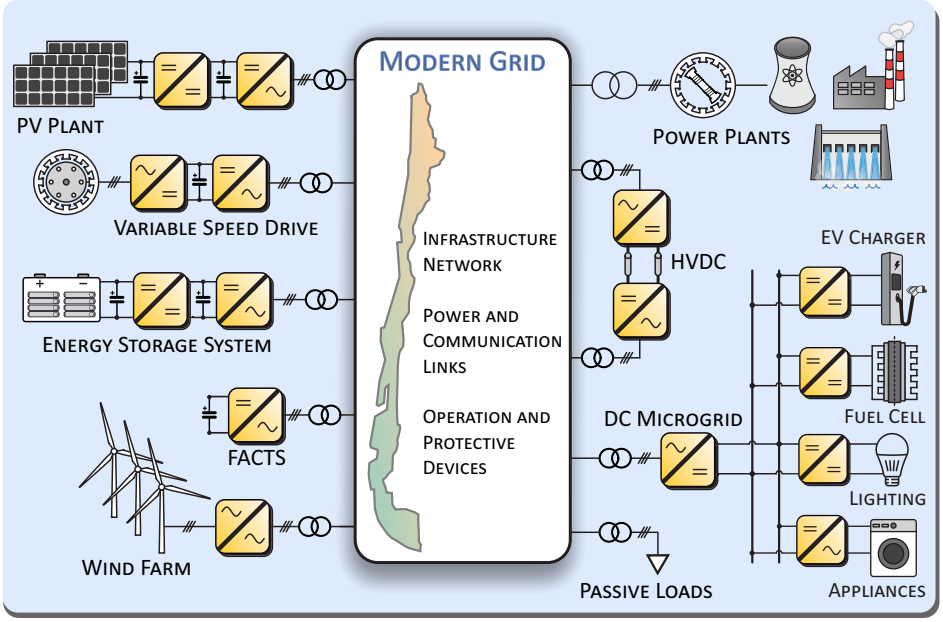

FIGURE 1.1: Power system with high penetration of power converters.

16, 17, 18, 19, 20, 21].

A particular type within MMCs family is the M2C Converter, whose topology is shown in Fig. 1.2, composed mainly of six branches that connect the phases through a line inductance to avoid short circuits and clusters of N half-bridge submodules, whose function is to synthesize the voltage required for a certain application. This converter is used to directly connect a DC port to an AC port where there is a variable speed drive, implying an application with a wide range of frequencies at the output port.

An inherent challenge of MMC converters is the complex task of their control, given the number of energy storage components they contain, combined with external requirements. This implies several control loops that may be dependent on each other. Thus, the control core focuses on the components that synthesize the voltage, namely, the voltage of each submodule (SM) and its corresponding capacitor.

In recent years, nested control systems based on decoupled modelling have been proposed in the literature for M2C topology. This methodology enables a decoupled control of input currents, output currents, and circulating currents [22, 23, 24]. In this regard, the control actions of each decoupled system do not interfere with each other, which enables performing the Inter-Cluster Balance (ICB) control and the Low-Frequency Oscillations (LFO) mitigation without affecting the external control systems.

These control stages are critical in the operation of a variable-speed drive since a common start-up involves passing through critical operating points with a low frequency at the output port, where the magnitude of the capacitor oscillation is inversely proportional to the frequency and directly proportional to the current of the AC port [25]. Therefore, it is essential to inject both circulating currents and common-mode voltage (CMV) at all times, with a dependence on these external variables. However, considering both variables entails a non-linear characteristic in the system that causes an impact between them and a consequent control that takes into

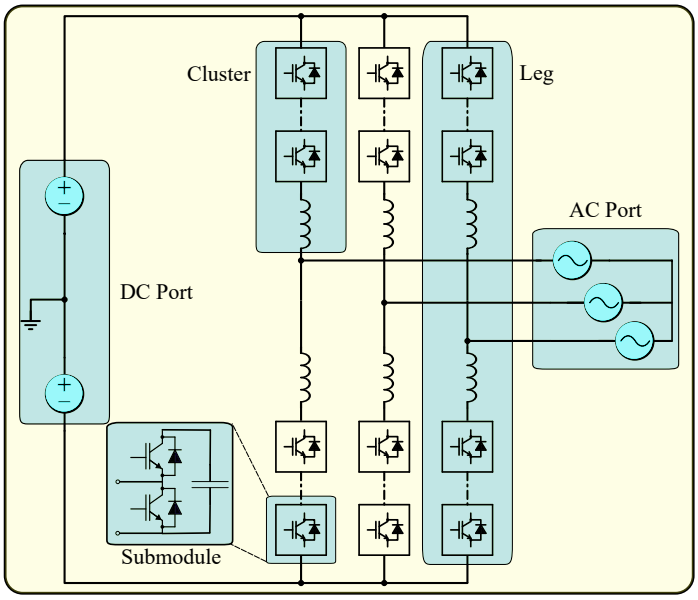

FIGURE 1.2: M2C Topology with half bridge as submodules.

account such nature of the problem. Moreover, in [26] the high demand for circulating currents in the converter is detailed as the power increases, especially for drives that use an M2C over the M3C. Regarding control, a frequently studied application is Model Predictive Control (MPC) [27], whose cost function solution depends on the dynamic model of the system and a prediction over a defined horizon. Its application allows for exceptional dynamic performance [28, 29, 30], coupled with its wide bandwidth particularly suited for variables without defined frequencies. For example, in [31], a continuous control set MPC (CCS-MPC) is introduced, formulating an optimization problem for the ICB and LFO stages where circulating current references are provided given a CMV signal. However, the control strategy does not consider the nonlinear model of energy in the clusters, leading to suboptimal solutions for the decision variables. Additionally, due to the computational resolution method, an extended prediction horizon cannot be achieved, limiting the ability to compensate voltage oscillations in a low-speed, high-torque drive.

To further increase MPC applicability, recent research has considered exploiting properties of optimization problems to improve computational efficiency. Thus, it becomes convenient for large-scale control applications, such as MMCCs, to split the original constrained optimal control problem (COCP) into a set of smaller and simpler subproblems. Active set [32, 33] and interior point methods [34, 35] are commonly employed in MPC, but for reduced computational complexity first order approaches such as fast gradient methods [36, 37] and alternating direction method of multipliers (ADMM) have received recent attention [38], being tested on a DC/AC converter with a hardware implementation[39].

Therefore, this work aims to improve the performance under conditions such as low-speed high-torque start by using a MPC Scheme on ICB and LFO control. The proposed MPC method is based on the Alternating Direction Method of Multiplier (ADMM) [38]. In essence, the ADMM is an algorithm that solves convex optimization problems by breaking them into smaller pieces, each of which are then easier to handle. Besides, To make better use of the

available computational capacity, the COCP is solved by considering an extended prediction horizon, which enhances the quality of the solution and, consequently, yields much more efficient ICB and LFO control.

1.1 Hypothesis and Objectives

The hypothesis of this thesis are:

1. The long-horizon MPC strategy based on the COCP proposed reduces voltage oscillations in the MMCCs by injecting optimal circulating currents.
2. The proposed decomposition strategy based on the Extended ADMM algorithm makes the proposed long-horizon MPC control strategy implementable in a real-time control platform for determining the optimal circulating currents references for MMCCs.
3. The implementation of an extended horizon allows for more efficient converter operation, reducing voltage oscillations with a lower magnitude current.
4. The proposed MPC strategy proposed can be applied to MMCC-based variable-speed drive applications, enabling a full frequency range operation.

The main objective of this project is to design and experimentally validate a Distributed Long-Horizon MPC strategy to achieve a more efficient control strategy that increases the operation range on High-Power Variable-Speed Drives by improving the ICB and LFO control tasks performance.

To achieve the main goal, the following challenges and specific goals have to be studied and accomplished through this project:

1. To design and develop a computationally efficient ADMM-Based algorithm to solve the overall COCP underlying the proposed linear MPC strategy, aiming to compute the optimal circulating currents in a real-time control platform.
2. To design and implement an experimental setup that incorporates a variable-speed drive based on the M2C topology.
3. To implement and experimentally validate the performance of the proposed MPC strategy in MMCC-based variable-speed drive applications.
4. To comprehensively assess the performance of the proposed control strategy under both steady-state and dynamic conditions.

2. Background

Behind the proposed control strategy, which has been subsequently validated, lies a theoretical foundation developed throughout the study in relevant fields such as power electronics, drives, and control theory, which incorporates optimization strategies in linear problems. Thus, this strategy can be applied to the reference generation in the energy balance control of the cascaded modular multilevel converter, incorporating the linear controls involved for the induction machine drive and the power balance between the converter's output and input, all modulated in the converter thanks to the PWM and Sorting Algorithm. Therefore, it is imperative to address all these concepts in detail as part of the background of this thesis.

2.1 The Modular Multilevel Cascaded Converters

The terms "modular" and "multilevel" are mainly used to refer to a power converters family characterized by the series connection of sub-modules (SM), usually based on half-bridges (HB) and full-bridges (FB) with floating DC-capacitors, as illustrated in Figs. 2.1(a)-(c). Thus, depending on the voltage level required by a specific application, the MMCC voltage rating can be easily enlarged by increasing the number of SMs per cluster N. Each SM contributes only a small voltage step and it can be controlled individually. As shown in Fig. 2.1(a), the cluster of N sub-modules connected in series and one inductor L constitute a branch (or arm), whose interconnections define specific topologies of the MMCCs family [11, 13]. For instance, the modular multilevel converter (M2C) is composed of six arms to interlink one DC-port to another three-phase AC system, as shown in Fig. 2.1(d). Even when the main applications of this topology are related to flexible HVDC transmission solutions [7, 40], since 2016 the M2C topology is also offered by Benshaw [41] and Siemens [42] as a commercial solution for medium-voltage drives. This latter takes advantage of the features of the cascaded topology to implement a cell bypass design [43] that cuts off the operation of a cell in case of failure without affecting the performance external tasks like speed and torque. Utilizing the converter's scalability, it provides redundancy of SM's that allow the voltage to be maintained even with

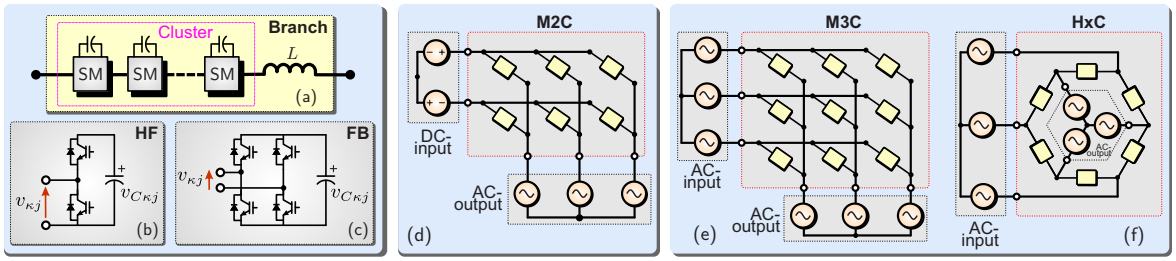

FIGURE 2.1: MMCC family topologies and SMs: (a) MMCC's branch; (b) half-bridge; (c) full-bridge; (d) M2C; (e) M3C; and (f) HxC.

failed cells, ranging from a 24-cell converter (4 per cluster) to a 66-cell converter (11 per cluster) composed of low-voltage IGBT semiconductors. Additionally, it offers one of the highest output power converters (∼47 MVA) with medium voltage up to 13.8 kV, being mainly recommended for driving pumps, fans, compressors, conveyors, etc. This is thanks to its ability to synthesize voltages over a wide range of magnitudes and frequencies.

On the other hand, the three-phase modular multilevel matrix converter (M3C), also known as triple-star bridge cell converter [13], interlinks two three-phase AC systems through nine branches, based on full-bridge SMs, as illustrated in Fig. 2.1(e). The M3C can also be used to directly interlink two single-phase AC systems (e.g. [44, 45, 46]). In addition, two AC three-phase systems can also be interfaced by the interconnection of six branches in a hexagonal configuration. This configuration, based on full-bridge SMs, is shown in Fig. 2.1(f) and it is also known as the Hexverter MMCC (HxC). It is important to highlight that the focus of this work is on the M2C converter due to its common use in drive applications.

2.2 Control Strategies for Modular Multilevel Cascaded Converters

MMCCs require many passive and active components to process electrical power, as shown in Fig. 2.1. Consequently, the control of MMCCs is complex and typically requires achieving several control tasks. Furthermore, these converters must not only govern variables at their input and output (I/O) ports, they must also control multiple internal variables. This multivariable control requirement is faced through various control loops, some dependent on each other and others independent, making them challenging to handle.

Among the control tasks to be performed, the control of the SM capacitor voltages is crucial to achieve a high-performance current control system, improving power quality indexes, such as reactive power and harmonics, and providing stability and safety.

In general, control strategies for any application of this family of converters can be divided into three-stage nested control loops applied to the SM capacitor voltages, as shown in Fig. 2.2, also considering the decoupling methods of the variables mentioned previously.

First, the external control systems provide the I/O current references $\boldsymbol{i}^*_{\text{ext}}$ to fulfill the requirements of a specific application (e.g., active and reactive power control for Low-Frequency AC (LFAC) systems or torque and speed control in drives). Also in the outer loops, the Total Energy Balancing (TEB) controller defines an active current component (from the input or output port) required to balance the overall MMCC's energy, namely i^*_{act}. The circulating current and the CMV references, $\boldsymbol{i}^*_z$ and v^*_0, respectively, are determined by the ICB and LFO controllers.

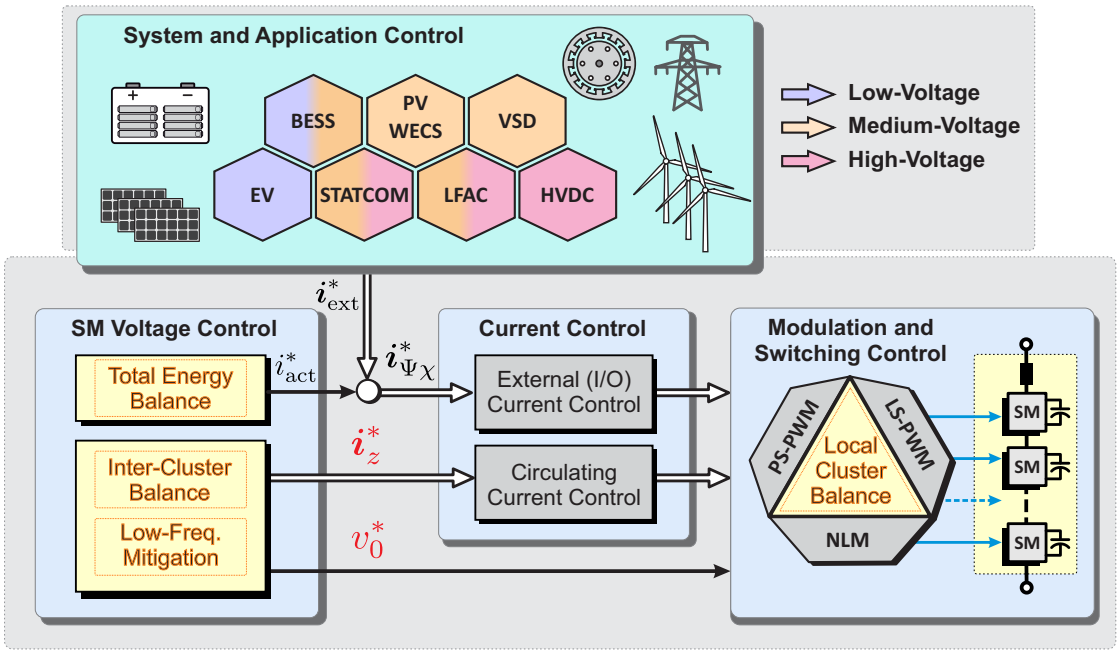

FIGURE 2.2: Control structure typically utilized for MMCCs

Second, thanks to the decoupled transformation, the I/O currents and the internal circulating currents are controlled independently because their control actions do not disturb each other. From this perspective, on the one hand, most of the external control systems are based on standard and well-known vector control techniques (e.g., field- and voltage-oriented control [47, 48]). On the other hand, proportional and multi-resonant controllers implemented in the transformed space (e.g., [49]) are usually utilized for the regulation of the circulating currents. Conversely, a constrained MPC strategy was recently introduced in [31] for M2Cs to perform the circulating current regulation in the transformed space ($\Sigma\Delta\alpha\beta 0$ framework).

Finally, in the third stage, the control actions of the decoupled models are mapped to the original coordinates by applying the inverse transformation. Once the cluster voltage references are obtained, the Local-cluster Balancing (LCB) control is locally performed in the modulation stage using differents approaches as shown in the Figure aforementioned and explained in more detail below.

2.2.1 Total Energy Balancing Control

The total energy balance control (TEB) is one of the most external controls within the multilevel converter schemes, as it performs the power balance between the input and output to ensure the appropriate amount of energy in the converter as a whole, allowing its operation in the other stages and tasks. In this regard, the control can be carried out using either the input or output current of the converter as the actuating variable. In the case of the M2C, the first variable is usually used since it is typically the source that provides power for the operation of a given application just like the focus of this work.

$$P_{M2C} = \frac{\mathrm{d}E_{M2C}}{\mathrm{d}t} = P_{DC} + P_{AC} \tag{2.1}$$

Now, the plant that directly derives from the power balance proposed in (2.1) has an integrator nature with a disturbance coming from the power of the output port. Thus, the direct relationship between the converter's energy and the actuation is as follows:

$$\frac{E_{M2C}(s)}{I_P(s)} = \frac{V_{dc}}{s} \tag{2.2}$$

For this reason, the action of a linear controller such as a PI-controller is sufficient to implement this balancing stage, taking into account the output power as a disturbance that must be compensated with feedforward techinque.

2.2.2 Inter-Cluster Balancing Control and Low-Frequency Oscillations Mitigation

Once the total energy of the converter is obtained, it must be distributed equally to each of the six clusters present in the M2C, ensuring that all reach the same average voltage value. Since this is an internal balance of the converter, the use of internal variables, such as circulating currents, is essential. The exclusive condition is that they do not affect the external controls; hence, they must not be reflected at the output and input ports. However, determining these signals is not a simple task as they consist of various components of specific frequencies and amplitudes according to the operating point.

While balancing between clusters through circulating currents is sufficient for a wide range of frequencies, it becomes complex in applications where the output frequency is very low, given its proximity to the fixed input frequency in an M2C. This is because the capacitor voltage magnitudes are amplified in this range of operation. Therefore, a common-mode voltage signal is injected as an additional degree of freedom to reduce oscillations for feasible operation. Outside of this range, this signal can be dispensed with as it generates side effects in the circulating currents and subsequent losses.

Most of the ICB control strategies reported in literature define a set of specific sinusoidal components of known frequencies for the circulating currents. However, the amplitudes of these components are hard to compute and optimize, and typically they are determined using open- and closed-loop strategies [50, 51, 52, 24]. For instance, in [50, 52] multiple proportional-integral controllers implemented in several synchronous reference frames rotating at $\omega_1 \pm \omega_2$ are used to determine the amplitudes of the set of pre-defined sinusoidal components for the circulating currents. Following this assumption, in [24], the amplitude of the circulating current components is computed by using an optimization criterion to minimize their amplitudes.

In [53], a branch current reallocation is proposed using a theoretical analysis to find an energy equilibrium of the M3C. Another MPC strategy was proposed in [54]. Here, the CMV and the circulating currents are obtained using an iterative algorithm. The CMV is first computed by minimizing a cost function with the quadratic sum of the tracking error of each cluster's equivalent capacitor voltage. Afterward, in the next iteration, the circulating currents are calculated by minimizing the same cost function but using the CMV computed in the previous step. An additional parameter depending on the output frequency is introduced to limit the injection of both CMV and circulating currents.

2.2.3 Local Cluster Balancing Control

The Local Cluster Balancing Control is the control that operates at the most detailed level in the converter, with the function of achieving the balance of the N_κ capacitors in their

respective submodules installed in each cluster. This control task is usually implemented on the modulation stage to locally control the capacitor voltage in every SM of each cluster. For doing this, two options are generally considered in the literature [51, 55]: (i) proportional controllers with the phase-shifted pulse-width modulation (PS-PWM) method or (ii) sorting algorithms with the level-shifted PWM (LS-PWM) or nearest level modulation (NLM) schemes [56]. Recently, MPC has also been proposed to deal with the balancing of the capacitor voltages in every cluster [57, 58]. For the purposes of this work's implementation, a hybrid LCB control approach has been utilized, in which some of the sub-converters are operating with PS-PWM method, while others utilize sort-and-select based LS-PWM.

Phase-shifted pulsed-width-modulation [55] is a technique in which the cluster voltage reference for a MMCC of N_κ SMs is modulated by a series of N_κ high frequency carrier waves, phase shifted $\frac{2\pi}{N_\kappa}$ from each other. For half-bridge-based SMs, the corresponding duty cycle d is directly modulated, whereas for full-bridge-based SMS, the duty cycle and its negative are both utilized. PS-PWM results in a natural intra-cluster balancing effect of the SMs capacitors in MMCCs operated through this technique [59]. As a result, the output voltage effective switching frequency of the cascaded converter becomes $2N_\kappa f_c$, with N_κ the number of SMs within each arm of the converter, and f_c the PWM carrier frequency. Additionally, this method can be regulated using proportional or proportional-integral controllers to consider active power deviation on the SMs.

An alternative approach is the Nearest Level Modulation (NLM) also known as Staircase modulation [60] which is applied when determining a on/off operation during the sampling period through the rounded value of the arm reference voltage. NLM method presents reduced power losses at the cost of higher harmonic distortion, albeit for very high voltage applications with hundred of SMs, the increased power quality with lower losses makes this the more attractive option [61].

As for LS-PWM [62], this technique considers N_κ multiple high frequency carrier waves, all of which are shifted in level to each other and compares them with arm voltage reference leading to the change of only one SMs voltage during the sampling period. This method has been noted for its improved voltage quality with reduced THD compared to PS-PWM [63]. Nevertheless, its implementation is not preferred over the PS-PWM for MMC due to the uneven switching frequency and conduction losses among SMs [64].

Both LS-PWM and NLM are often implemented together with an sorting method to achieve the local cluster balance. The sorting is based on a priority list considering the voltage of each SMs and the current sign at each sample time. Thus, the imbalance is regulated operating the SMs with higher voltage in discharge state or the SMs wih lower voltage in charge state. Therefore, the algorithm should be fast to avoid scalability issues when N_κ increase leading to more time to perform the order[65].

2.2.4 Branch Current Control

With the exception of the LCB control, all other schemes must pass through a current control stage as an intermediate step before obtaining the reference voltages. By using transformations to other frameworks, the current controls (Input-Output-Circulating) are performed separately and independently, due to the frequency requirements needed for each one and to consider the dynamic phenomena such as in induction machine drives[66, 67, 50, 54, 24].
Thus, this work will rely on this approach to carry out this stage, using linear controllers for the DC port responsible for TEB control and the AC port responsible for machine control,

while the reference circulating currents generated by the proposed algorithm will be controlled using CCS-MPC, as it is a technique that allows reference tracking over a wide frequency range[31, 25].

2.3 Continuous–Control–Set Model Predictive Control

In the last decade, MPC has surged as one of the most studied topics for control of power electronic systems [27, 68]. In all of its different forms, MPC follows a rather simple approach. A constrained optimal control problem (COCP) is formulated, in which the optimal control input is an optimization variable that minimizes a cost function depending on the predicted dynamical behavior of the system states and inputs in a given prediction horizon. By repeatedly solving the aforementioned optimization problem in real time and only using the control variable until a given control horizon, a principle known as the receding horizon policy introduces feedback to the system.

As the name of the control method implies, *model predictive* control depends on a given system model based on which predictions can be made for the dynamical behavior of the system. In general, let us denote the state vector of the system as $\boldsymbol{x}$, the input vector as $\boldsymbol{u}$ and the system output as $\boldsymbol{y}$. In the continuous-time domain, the dynamic model of the system takes the form:

$$\frac{\mathrm{d}\boldsymbol{x}(t)}{\mathrm{d}t} = \boldsymbol{f}(\boldsymbol{x}(t), \boldsymbol{u}(t)) \tag{2.3a}$$

$$\boldsymbol{y}(t) = \boldsymbol{h}(\boldsymbol{x}(t), \boldsymbol{u}(t)) \tag{2.3b}$$

In which (2.3a) is the differential equation that represents the system's continuous dynamic, while (2.3b) maps the system's output variables to its states and inputs. From this generalized nonlinear system model, a discrete-time model can be determined, through Forward-Euler approximation [68], or, for a linear or linearized system, through exact discretization.

$$\boldsymbol{x}(k+1) = \boldsymbol{F}(\boldsymbol{x}(k), \boldsymbol{u}(k)) \tag{2.4a}$$

$$\boldsymbol{y}(k) = \boldsymbol{G}(\boldsymbol{x}(k), \boldsymbol{u}(k)) \tag{2.4b}$$

This discrete model is often, but not necessarily, a linear model in which the functions $\boldsymbol{F}$ and $\boldsymbol{G}$ can be expressed as linear combinations of the system states and inputs. It should be noted that depending on the model utilized, the system inputs $\boldsymbol{u}(k)$ can either be continuous control input references, or discrete states.

In power electronics, the use of the discrete switching state as the control inputs in the model is known as Finite-Control-Set MPC (FCS-MPC), which eliminates the need for a modulation stage in the control scheme of the converter, but results in a constrained optimization problem with a discrete set of feasible values (integer or not), requiring the use of mixed integer linear programming techniques. If instead, the system voltages are calculated as continuous values and subsequently modulated into the switching inputs, this strategy is known as Continuous-Control-Set MPC (CCS-MPC), and is the basic strategy considered in this work, in which quadratic programming algorithms can be utilized [69, 70]. Both of these distinct model predictive control strategies, as well as specific variants of each are shown in Fig. 2.3.

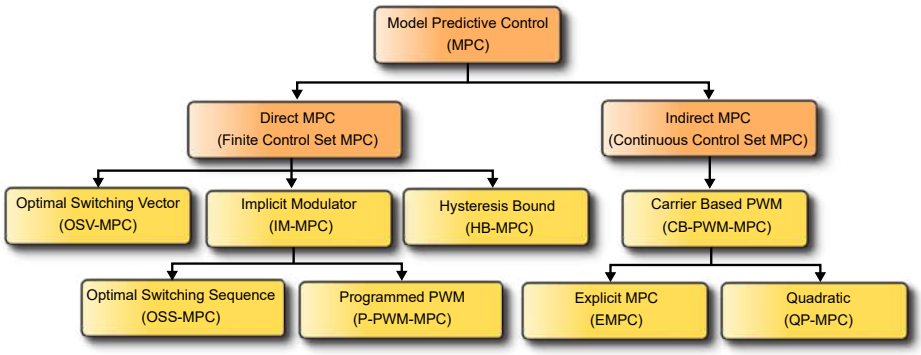

FIGURE 2.3: Classification of MPC strategies applied to power converters and drives [1].

Vectors for the optimal inputs and predicted states and outputs over the prediction horizon can be established, all of which are related through the discrete-time model presented in (2.4):

$$\boldsymbol{U}(k) = \begin{bmatrix}\boldsymbol{u}(k) & \boldsymbol{u}(k+1) & \dots & \boldsymbol{u}(N_p-1)\end{bmatrix}^T$$
$$\boldsymbol{X}(k) = \begin{bmatrix}\boldsymbol{x}(k+1) & \boldsymbol{x}(k+2) & \dots & \boldsymbol{x}(N_p)\end{bmatrix}^T$$
$$\boldsymbol{Y}(k) = \begin{bmatrix}\boldsymbol{y}(k+1) & \boldsymbol{y}(k+2) & \dots & \boldsymbol{y}(N_p)\end{bmatrix}^T$$

The proper selection of a control function is required and fundamental for the accomplishment of the desired control tasks, and is a non-trivial problem. However, in general, most cost functions can be established as:

$$J(\boldsymbol{x}(k), \boldsymbol{u}(k)) = \sum_{\ell=0}^{N_p-1} \mathcal{J}(\boldsymbol{x}(\ell+1), \boldsymbol{u}(\ell)) + \mathcal{J}_0(\boldsymbol{x}(0))$$

In which $\mathcal{J}$ is a scalar stage cost function that depends on the predicted states and control inputs in a given instant ℓ as per the discrete-time mode, and is formulated as a penalizing performance index, such as the square norm error of the output respect to its reference value. Given that the predicted system states depend exclusively on the known initial state $\boldsymbol{x}(0)$ and the input variables $\boldsymbol{u}(k)$, the argument of the cost function is the system input that becomes the optimization variable. In general, the constrained optimal control problem is then formulated as:

$$\min_{\boldsymbol{u}(k)} \quad J = \sum_{\ell \in \mathcal{H}} \mathcal{J}(\boldsymbol{x}(\ell+1), \boldsymbol{u}(\ell)) + \mathcal{J}_0(\boldsymbol{x}(0)) \tag{2.5a}$$
$$\text{s.t.} \quad \boldsymbol{x}(k+1) = \boldsymbol{F}(\boldsymbol{x}(k), \boldsymbol{u}(k)) \tag{2.5b}$$
$$\boldsymbol{y}(k) = \boldsymbol{G}(\boldsymbol{k}(k), \boldsymbol{u}(k)) \tag{2.5c}$$
$$\boldsymbol{u}(\ell) \in \mathcal{U} \tag{2.5d}$$
$$\boldsymbol{x}(\ell+1) \in \mathcal{X} \tag{2.5e}$$
$$\boldsymbol{y}(\ell+1) \in \mathcal{Y}, \quad \forall \ell \in \mathcal{H} = \{0, 1, \dots, N_p - 1\} \tag{2.5f}$$

where the general constraints for the system states, inputs and outputs are also explicitly included. These constraints ensure that the optimal solutions found are feasible according to

the physical reality and operational range of the system, as well as making sure that the states and outputs remained controlled inside the feasible range during all of the prediction horizon. The capacity to explicitly include constraints in potentially nonlinear systems where multiple inputs and outputs are coupled together and must be simultaneously controlled is one of the advantages of MPC as a control strategy in general.

2.4 Constrained Quadratic Programming Problem

The field of optimization has an ever growing importance on the sciences, economics, industry and engineering [71, 72, 73, 74]. There are multiple subfields of optimization depending on the different problems that require to be solved. In particular, for power electronics the increased interest in CCS-MPC has given rise to constrained continuous optimization problems that must be solved efficiently in real time. Depending on the nature of objective function and the constraints, different algorithms can be selected to efficiently solve a given problem. For constrained problems in particular, the existence of unequality constraints introduces an additional challenge, as the algorithm must determine the set of active constraints that must be satisfied to ensure optimality and feasability, presenting a combinatorial difficulty problem [73].

In general, the optimization function appears as a quadratic function which is solve via active-set method when there are constraints to be considered. However, the same problem can be solved by decomposition into subproblems as the method presented in this work, the alternating direction method of multiplier (ADMM) optimization algorithm.

2.4.1 Quadratic Programming

Optimization problems that present a quadratic cost function and linear constraints are known as quadratic programming (QP) problems [73]. These problems appear often in different contexts, such as in the most common cost functions associated to CCS-MPC for power electronics. They can also appear as subproblems associated to algorithms implemented for more difficult problems, such as sequential quadratic programming (SQP), augmented Lagrangian methods and interior point methods [73]. In general, a QP problem can be defined as:

$$\min_{\boldsymbol{x}} \quad J(\boldsymbol{x}) = \frac{1}{2}\boldsymbol{x}^T\mathbf{H}\boldsymbol{x} + \boldsymbol{f}^T\boldsymbol{x} \tag{2.6a}$$

$$\text{s.t.} \quad \mathbf{A}\boldsymbol{x} \leqslant \boldsymbol{b} \tag{2.6b}$$

$$\mathbf{C}\boldsymbol{x} = \boldsymbol{d} \tag{2.6c}$$

In which $\boldsymbol{x}$ and $\boldsymbol{f}$ are vectors belonging to $\mathbb{R}^n$, $\boldsymbol{b}$ belongs to $\mathbb{R}^m$, $\boldsymbol{d}$ belongs to $\mathbb{R}^p$, while $\mathbf{H}$, $\mathbf{A}$ and $\mathbf{C}$ are $n \times n$, $m \times n$ and $p \times n$ size matrices, respectively. QP problems can always reach a solution (or determine infeasibility) in finite time, which depends on the nature of the objective function and the size of the inequality constraints. When the Hessian matrix $\mathbf{H}$ is positive definite, the QP problem is convex and of similar difficulty to linear programming (LP) problems. Furthermore, if the problem is unconstrained (or there are no active constraints and all of the equality constraints have been eliminated), the optimal unconstrained solution can be found as:

$$\boldsymbol{x} = -\mathbf{H}^{-1}\boldsymbol{f} \tag{2.7}$$

Whereas if the $\mathbf{H}$ matrix is indefinite, the problem turns nonconvex and can present stationary points and local minima, making for a more challenging problem to solve [73]. There are several methods available to solve QP problems presenting both equality and inequality constraints, such as active-set, interior-point, augmented Lagrangian, amongst others [73]. In particular, for small and medium size problems, active-set methods have shown to be effective in estimating the optimal active set and solution.

2.4.2 Active-Set Methods

In general, unconstrained QP problems can be directly solved without recurring to iterative algorithms. As for equality constrained QP problems, it has been shown that through different techniques, they can be often transformed into equivalent reduced unconstrained problems, depending on the particular equality constrains present. For inequality constrained problems, however, the problem of determining the active set of inequality constraints (in which they can be considered as equality constraints) becomes the main challenge. Active-set approaches, such as the well-known simplex method [73] for LP problems tries to make guesses for the active set of inequalities and iteratively updating the set until reaching optimality conditions.
For QP problems, the active-set methods works in a similar fashion, although unlike the simplex method, the iterates and the optimal solution can be found outside the vertices of the feasible solution space. Let us consider a primal active-set method, in which, at each iterate a equality-constrained QP subproblem is solved, considering some inequality constraints active and all the original equality constraints present, together known as the working set.
For the kth iterate, we consider a working set $\mathcal{W}_k$ and a solution $\boldsymbol{x}_k$. The algorithm starts from a given feasible starting point $\boldsymbol{x}_0$ and setting $\mathcal{W}_0$ as a subset of the active constraints for this starting point. First, it minimizes a quadratic subproblem, and checks whether the solution is found within the feasible region defined by the working set. If it does not, a step is calculated solving the working set-equality constrained QP subproblem without considering the inactive inequality constraints [73]. This subproblem can be expressed in terms of the step $\boldsymbol{p}$ by:

$$\boldsymbol{p} = \boldsymbol{x} - \boldsymbol{x}_k\,, \qquad \boldsymbol{g}_k = \mathbf{H}\boldsymbol{x}_k + \boldsymbol{f}$$

In this way, the cost function can be written as:

$$J(\boldsymbol{x}) = J(\boldsymbol{x}_k + \boldsymbol{p}) = \frac{1}{2}\boldsymbol{p}^T\mathbf{H}\boldsymbol{p} + \boldsymbol{g}_k^T\boldsymbol{p} + \underbrace{\left(\frac{1}{2}\boldsymbol{x}_k^T\mathbf{H}\boldsymbol{x}_k + \boldsymbol{f}^T\boldsymbol{x}_k\right)}_{:=\rho_k}$$

where the term ρ_k does not depend on the step $\boldsymbol{p}$. In this way, if $\boldsymbol{p}$ is selected as optimization variable, the term can be dropped and the following QP subproblem can be formulated:

$$\min_{\boldsymbol{x}} \quad \frac{1}{2}\boldsymbol{p}^T\mathbf{H}\boldsymbol{p} + \boldsymbol{g}_k^T\boldsymbol{p} \tag{2.8a}$$

$$\text{s.t.} \quad \mathbf{C}_{\mathcal{W}}\boldsymbol{p} = \mathbf{0} \tag{2.8b}$$

in which $\mathbf{C}_{\mathcal{W}}$ is a $(p + m_{\mathcal{W}}) \times n$ matrix corresponding to the p equality constraints and the $m_{\mathcal{W}}$ active inequality constraints. The solution to this subproblem is denoted as $\boldsymbol{p}_k$. It can be noted that as $\mathbf{C}_{\mathcal{W}}\boldsymbol{p}_k = \mathbf{0}$, the active set remains the same, that is, the constraints for $\mathbf{C}_{\mathcal{W}}\boldsymbol{x}_k$ will be also satisfied for $\mathbf{C}_{\mathcal{W}}(\boldsymbol{x}_k + \alpha\boldsymbol{p}_k)$, for any value taken by α. Once the step $\boldsymbol{p}_k$ is computed, the next iterate is obtained through

$$\boldsymbol{x}_{k+1} = \boldsymbol{x}_k + \alpha_k \boldsymbol{p}_k \tag{2.9}$$

Where α_k is the largest value the parameter can take in [0, 1] such that all constraints are satisfied. By this, we refer to the inequality constraints that remain outside the working set, as all the working set constraints are always satisfied in each iterate. If this value results less than 1, then some of there are considered blocking constraints, and after the iterate, a new working set $\mathcal{W}_{k+1}$ is defined by adding one of the blocking constraints to the previous working set. This method is iteratively repeated until a solution for the quadratic cost function minimization $\boldsymbol{x}^*$ is found within in the region defined by the working set $\mathcal{W}^*$. In this point, the step subproblem (2.8) has solution zero.

2.4.3 Alternating Direction Method of Multiplier Algorithm

According to [75], the ADMM algorithm aims to solve the general QP problem in (2.6) which can be rewritten considering a separable function:

$$\min_{\boldsymbol{x}} \quad J(\boldsymbol{x}) = \sum_{\kappa \in \mathcal{K}} J_\kappa(\boldsymbol{x}_\kappa) \tag{2.10a}$$

$$\text{s.t.} \quad \mathbf{A}\boldsymbol{x} \leqslant \boldsymbol{b} \tag{2.10b}$$

$$\sum_{\kappa \in \mathcal{K}} \mathbf{C}_\kappa \boldsymbol{x}_\kappa = \boldsymbol{d} \tag{2.10c}$$

Where $\mathcal{K} = \{1, 2, \ldots, m\}$ represents the m separable functions in $J(\boldsymbol{x})$ that are defined by blocks of $\boldsymbol{x}_\kappa$ variables in such a way that $\boldsymbol{x} = [\boldsymbol{x}_1 \ \boldsymbol{x}_2 \ \cdots \ \boldsymbol{x}_m]^\intercal$. Accordingly, the constraint (2.10c) should be written in terms of these variables, leading to the definition of matrices $\mathbf{C}_\kappa$. Then, the iterative method is applied as follows:

$$\boldsymbol{x}_1^{(n+1)} = \arg\min_{x_1 \in \mathcal{X}_1} \mathcal{L}_\rho(\boldsymbol{x}_1, \boldsymbol{x}_2^{(n)}, \ldots, \boldsymbol{x}_m^{(n)}, \lambda^{(n)}) \tag{2.11a}$$

$$\boldsymbol{x}_2^{(n+1)} = \arg\min_{x_2 \in \mathcal{X}_2} \mathcal{L}_\rho(\boldsymbol{x}_1^{(n+1)}, \boldsymbol{x}_2, \ldots, \boldsymbol{x}_m^{(n)}, \lambda^{(n)}) \tag{2.11b}$$

$$\vdots \quad \vdots$$

$$\boldsymbol{x}_m^{(n+1)} = \arg\min_{x_m \in \mathcal{X}_m} \mathcal{L}_\rho(\boldsymbol{x}_1^{(n+1)}, \boldsymbol{x}_2^{(n)}, \ldots, \boldsymbol{x}_m, \lambda^{(n)}) \tag{2.11c}$$

$$\lambda^{(n+1)} = \lambda^{(n)} - \rho \left(\sum_{\kappa \in \mathcal{K}} \mathbf{C}_\kappa \boldsymbol{x}_\kappa^{(n+1)} - \boldsymbol{d} \right) \tag{2.11d}$$

Here n represents the iteration counter, λ is the dual variable, $\rho > 0$ is a parameter used to penalizes the violation of the linear constraint, and $\mathcal{L}_\rho(\cdot)$ denotes the augmented Lagrangian derived from (2.10), which is presented in (2.12). Thus, the algorithm is straightforward, consisting of a sequential optimization of the primal variables $\boldsymbol{x}_\kappa$ followed by a dual variable update as shown in (2.11d). One of the main features of this algorithm is that it converges to the globally optimal solution when all the functions J_κ are strongly convex [76, 77]. Additionally, the ADMM algorithm allows utilizing the fact that the cost function is separable into the terms J_κ without affecting the convergence of the overall problem [38]. Thus, terms not related to the variable of the κth cluster could be omitted.

$$\mathcal{L}_\rho(\boldsymbol{x}_\kappa, \lambda) = \sum_{\kappa\in\mathcal{K}} (J_\kappa(\boldsymbol{x}_\kappa) - \lambda^\intercal \mathbf{C}_\kappa \boldsymbol{x}_\kappa) + \frac{\rho}{2} \| \sum_{\kappa\in\mathcal{K}} \mathbf{C}_\kappa \boldsymbol{x}_\kappa - \boldsymbol{d}\|^2 \tag{2.12}$$

It should be noted that the constraint (2.10b) is considered when solving each subproblem, depending on whether it is active. Moreover, the algorithm itself allows for closed-form analytical solutions given the function being optimized, thereby reducing the computational burden of each iteration. Nevertheless, a disadvantage of algorithm (2.11) is that it updates primal variables sequentially, making it unsuitable for parallelization. Recently, proximal algorithms have been introduced in literature to overcome this drawback [78, 79]. However, the thesis will focus on implement and evaluate the alternating algorithm given by (2.11).

2.4.4 ADMM algorithm convergence

The iterative algorithm that will be executed at each sampling instance requires a convergence criterion to stop and give the reference to the Current Controller. According to [75], two criteria can be established as given by (2.13), which consider the feasibility of the solution and its optimality, respectively. Thus, it is possible to consider the approaches separately, taking into account the reduction in computation time. In this regard, there will be a trade-off between choosing feasibility over optimality due to its convergence rate.

$$\max_{\kappa\in\mathcal{K}} \left\{ \left\| \sum_{\kappa\in\mathcal{K}} \mathbf{C}_\kappa \boldsymbol{x}_\kappa^{(n)} - \boldsymbol{d} \right\|, \ \| \mathbf{C}_\kappa \boldsymbol{x}_\kappa^{(n)} - \mathbf{C}_\kappa \boldsymbol{x}_\kappa^{(n+1)} \| \right\} \leqslant \varepsilon \tag{2.13}$$

In this regard and as a complement, [38] define two terms as primal and dual residuals as shown in (2.14a) and (2.14b) respectively which are derived from the primal and dual feasibility conditions. Therefore, this residuals serve as sufficient conditions to converge to the optimal solution of the COCP as iterations increase, with the only consideration that J_κ are proper, closed, and convex functions, even without conditions on the matrix $\mathbf{C}$ such as being full rank.

$$r^{n+1} = \mathbf{C}_\kappa \boldsymbol{z}_\kappa^{(n)} \tag{2.14a}$$

$$s^{n+1} = \rho \mathbf{C}_\kappa \left(\boldsymbol{x}_\kappa^{(n+1)} - \boldsymbol{x}_\kappa^{(n)} \right) \tag{2.14b}$$

Moreover, the parameter ρ fulfils the same objective of balance between optimality and feasibility since the higher value of this parameter places greater emphasis on satisfying the null space constraint over minimizing $J(\boldsymbol{x})$. Nevertheless, this work considers convergence through the primal residual $r^{(n)}$ as the initial approach and which coincides with the first criterion of (2.13).

2.5 Field Oriented Control of Induction Machines

Regarding energy control, low-speed medium voltage drives are among the most demanding applications for MMCC technologies. The low-frequency output combined with high torque leads to significant cluster energy imbalances, making both the ICB and LFO control tasks particularly challenging. This imbalance presents an operational limitation when choosing the topology for such applications, exemplified by the low-speed mills used in mining processing. The control strategy proposed in this work aims to address these challenges by fully and optimally

utilizing all available degrees of freedom, named common-mode voltage and circulating currents, and its performance will be evaluated for these specific applications.
Accordingly, the induction machine drive is chosen for its conventional use and extensive theoretical background. Moreover, as mentioned in previous sections, linear controllers are opted for, with the most commonly used in these drives being Direct Torque Control (DTC) and Field-Oriented Control (FOC). The latter will be explained below and used for this work.

2.5.1 Dynamical Model of the Induction Machine

For the generalized asynchronous machine, the dynamical behavior of the electrical system can be modelled by the following equations in the synchronous rotating reference frame ω_s, in which there are four complex variables ($\boldsymbol{i}_s, \boldsymbol{i}_r, \boldsymbol{\psi}_s, \boldsymbol{\psi}_r$), as well as two input voltages ($\boldsymbol{v}_s$ and $\boldsymbol{v}_r$), also the machine schaft rotates at speed ω:

$$\boldsymbol{v}_s = R_s \boldsymbol{i}_s + \frac{\mathrm{d}\boldsymbol{\psi}_s}{\mathrm{d}t} + j\omega_s \boldsymbol{\psi}_s \tag{2.15a}$$

$$\boldsymbol{v}_r = R_r \boldsymbol{i}_r + \frac{\mathrm{d}\boldsymbol{\psi}_r}{\mathrm{d}t} + j(\omega_s - \omega) \boldsymbol{\psi}_r \tag{2.15b}$$

$$\boldsymbol{\psi}_s = L_s \boldsymbol{i}_s + L_{sr} \boldsymbol{i}_r \tag{2.15c}$$

$$\boldsymbol{\psi}_r = L_{rs} \boldsymbol{i}_s + L_r \boldsymbol{i}_r \tag{2.15d}$$

Where R_s and L_s denotes the stator resistance and inductance as well as R_r and L_r for rotor side, besides, the mutual inductance is represented by $L_{sr} = L_{rs} = L_m$. On the other hand, the mechanical system of this drive, considering any mechanical load, is dynamically modeled according to the following equation:

$$T_e + T_L = \frac{J}{p} \frac{\mathrm{d}\omega}{\mathrm{d}t} + \frac{D}{p} \omega \tag{2.16}$$

Being J the inertia, p the pair poles of the machine and D the damping factor. Additionally, the electromagnetic torque is defined according to (2.17), forming a system of nonlinear equations which, however, can be controlled by choosing an appropriate rotating reference frame such as the synchronous speed frame. This allows dynamic control to achieve constant values in steady state using linear control strategies.

$$T_e = -\frac{3p}{2} \operatorname{Im}\{\boldsymbol{\psi}_s \boldsymbol{i}_s^*\} \tag{2.17}$$

Although the complete electrical system of the induction machine defined in (2.15) has four different variables, only two of these equations are differential, while the flux linkage equations are merely algebraic. Due to this, the electrical system can be reduced to a set of only two explicit variables, being the choice of these variables a degree of freedom depending on the given application. A common control strategy is based on the selection of one flux linkage variable and one current variable to model the system.
Such is the case for the squirrel-cage induction machine (SCIM). As the rotor of this machine is unavailable, all measurements and control are made on the stator side. In particular, the most direct variable for such task is the stator current $\boldsymbol{i}_s$. Through measurements of this variable and the rotor speed ω, the rotor flux linkage $\boldsymbol{\psi}_r$ can be also estimated, being these two the controlled and state variables of the system. With this selection, the electromechanical system is modelled by:

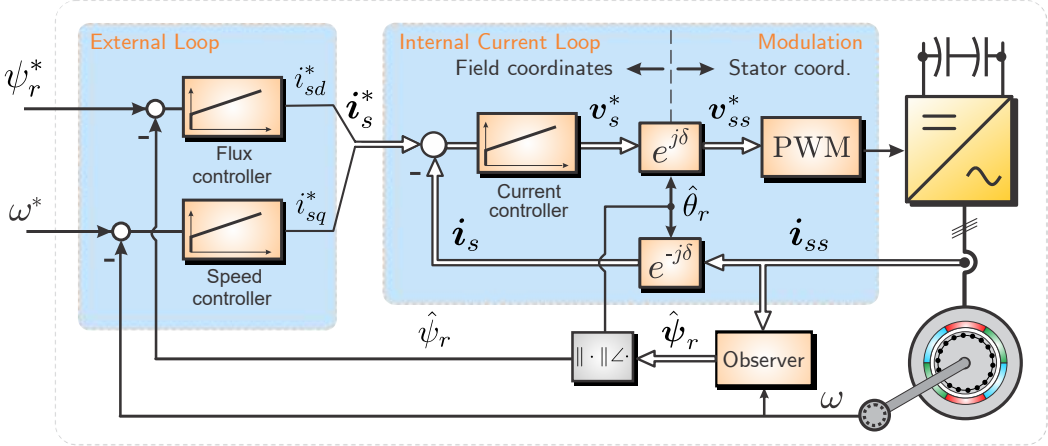

FIGURE 2.4: Field Oriented Control (FOC) control scheme for induction machine drive, controlling speed and flux [2].

$$\tau_\sigma \frac{\mathrm{d}\boldsymbol{i}_s}{\mathrm{d}t} + \boldsymbol{i}_s = \frac{1}{R_\sigma}\left(-j\omega_s L_\sigma \boldsymbol{i}_s - \left(j\omega - \frac{1}{\tau_r}\right) k_r \boldsymbol{\psi}_r + \boldsymbol{v}_s\right) \tag{2.18a}$$

$$\tau_r \frac{\mathrm{d}\boldsymbol{\psi}_r}{\mathrm{d}t} + \boldsymbol{\psi}_r = -j\omega_r \tau_r \boldsymbol{\psi}_r + L_m \boldsymbol{i}_s \tag{2.18b}$$

$$\frac{\mathrm{d}\omega}{\mathrm{d}t} = \frac{p}{J}\left(k_T \operatorname{Im}\{\boldsymbol{\psi}_r^* \boldsymbol{i}_s\} - T_L\right) \tag{2.18c}$$

Where $L_\sigma = \sigma L_s$, $R_\sigma = R_s + k_r^2 R_r$, $\tau_\sigma = \frac{L_\sigma}{R_\sigma}$, $\tau_r = \frac{L_r}{R_r}$ and $k_T = \frac{3}{2} p k_r$. The reduced system presented in (2.18) considers the stator current and rotor flux linkage as first-order systems with time constant τ_σ and τ_r, respectively. The first of these, presented in (2.18a), is considerably faster, allowing for dynamically decoupled control loops in terms of their frequency. It can be noted that the stator current system has the stator voltage $\boldsymbol{v}_s$ as a direct control input, whereas, once controlled, the stator current itself becomes an input for the rotor flux.

2.5.2 Field-Oriented Control

When the dynamical system's reference frame is oriented with the rotor flux linkage variable $\boldsymbol{\psi}_r$, the quadrature component by definition is null, that is:

$$\boldsymbol{\psi}_r = \psi_{rd}$$

With this consideration, the electromechanical system in (2.18) can be rewritten, separating direct and quadrature components as:

$$\tau_\sigma \frac{\mathrm{d}i_{sd}}{\mathrm{d}t} + i_{sd} = \frac{1}{R_\sigma}\left(\omega_s L_\sigma i_{sq} + \frac{k_r}{\tau_r}\psi_{rd} + v_{sd}\right) \tag{2.19a}$$

$$\tau_\sigma \frac{\mathrm{d}i_{sq}}{\mathrm{d}t} + i_{sq} = \frac{1}{R_\sigma}\left(-\omega_s L_\sigma i_{sd} - \omega k_r \psi_{rd} + v_{sq}\right) \tag{2.19b}$$

$$\tau_r \frac{\mathrm{d}\psi_{rd}}{\mathrm{d}t} + \psi_{rd} = L_m i_{sd} \tag{2.19c}$$

$$\omega_r \tau_r \psi_{rd} = L_m i_{sq} \tag{2.19d}$$

$$\frac{\mathrm{d}\omega}{\mathrm{d}t} = \frac{p}{J}\left(k_T \psi_{rd} i_{sq} - T_L\right) \tag{2.19e}$$

This allows for control through a nested system shown in Fig.2.4, where the inner control corresponds to the stator current in the direct and quadrature axes according to equations (2.19a) and (2.19b). Both regulate an external variable such as the rotor flux through the direct axis current according to (2.19c) and the rotational speed through the quadrature current, whose relationship with the electromagnetic torque is directly proportional according to equation (2.19e). The tuning of each plant involved in the control system must be done considering the dynamics of the variables involved to avoid generating undesirable dynamic responses and to achieve good reference tracking.

2.5.3 Flux Estimation

The most important element that enables the aforementioned control strategy is being able to work with the variables in a reference frame that is oriented with the rotor flux linkage. In practice, measuring the actual rotor flux linkage is not a feasible option due to different economical and technical difficulties. Thus, indirect methods to compute this variable should be considered.

2.5.3.1 Rotor machine model based estimator

With the aforementioned in consideration, a model to estimate the rotor flux linkage as to enable the FOC strategy is absolutely required. Different models have been proposed with different degrees of precision and distinct applications. This work will employ a estimator based on the rotor model of the machine using the synchronous frame ω_s. Fig. 2.5 illustrates the block diagram to obtain both flux angle and magnitude.

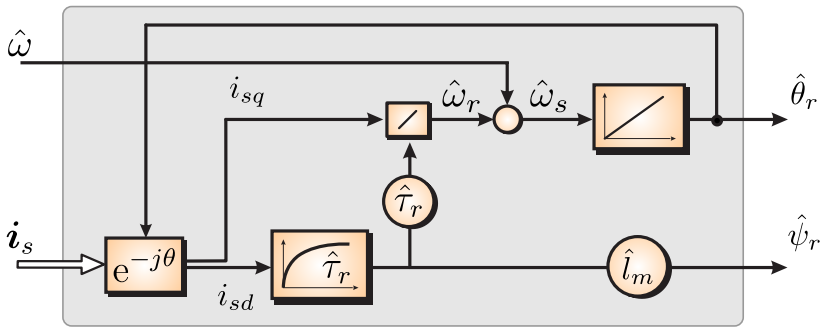

FIGURE 2.5: Current Model Flux Estimator based on rotor machine model [2].

This model is fully dependent on the rotor time constant τ_r and mutual inductance L_m which are

usually estimated and causes small errors taking into account the variation of these parameters in certain operating points.

2.5.3.2 Kalman Filter based estimator

Another robust estimator is based on stationary-state Kalman filter where the state-space model of the machine must be formulated in a stationary reference frame as follows:

$$\frac{\mathrm{d}}{\mathrm{d}t}\underbrace{\begin{bmatrix}\boldsymbol{i}_s\\ \boldsymbol{\psi}_r\end{bmatrix}}_{\boldsymbol{x}} = \underbrace{\begin{bmatrix}\mathbf{A}_{11} & \mathbf{A}_{12}(\omega)\\ \mathbf{A}_{21} & \mathbf{A}_{22}(\omega)\end{bmatrix}}_{\mathbf{A}(\omega)}\begin{bmatrix}\boldsymbol{i}_s\\ \boldsymbol{\psi}_r\end{bmatrix} + \underbrace{\begin{bmatrix}\mathbf{B}_1\\ \mathbf{0}\end{bmatrix}}_{\mathbf{B}}\boldsymbol{v}_s \tag{2.20a}$$

$$\boldsymbol{y} = \underbrace{\begin{bmatrix}\mathbf{I} & \mathbf{0}\end{bmatrix}}_{\mathbf{C}}\begin{bmatrix}\boldsymbol{i}_s\\ \boldsymbol{\psi}_r\end{bmatrix} \tag{2.20b}$$

This model is discretized for implementation in the equation (2.21) observer with a sampling time T_s for each instant k. The advantage of this observer is that it operates as a closed-loop system that ensures good performance, always under the consideration of a system that satisfies the observability condition.

$$\hat{\boldsymbol{x}}(k+1) = \mathbf{A}_d\hat{\boldsymbol{x}}(k) + \mathbf{B}_d\boldsymbol{v}_s(k) + \mathbf{K}_F(\boldsymbol{y}(k) - \mathbf{C}\hat{\boldsymbol{x}}(k)) \tag{2.21}$$

where:

$$\mathbf{A}_d = \mathbf{I}_4 + \mathbf{A}T_s + \frac{T_s^2}{2}\mathbf{A}^2$$
$$\mathbf{B}_d = \left(\mathbf{I}_4 T_s + \frac{T_s^2}{2}\mathbf{A}\right)\mathbf{B}$$

Furthermore, the distinctive feature of the Kalman filter lies in its gain $\mathbf{K}_F$, which is determined by the Riccati matrix equation:

$$\mathbf{K}_F = \mathbf{A}_d\mathbf{P}\mathbf{C}^\intercal\left(\mathbf{C}\mathbf{P}\mathbf{C}^\intercal + \mathbf{R}\right)^{-1} \tag{2.22a}$$
$$\mathbf{P} = \left(\mathbf{A}_d - \mathbf{K}_F\mathbf{C}\right)\mathbf{P}\mathbf{A}_d^\intercal + \mathbf{Q} \tag{2.22b}$$

Here, the matrices $\mathbf{Q}$ and $\mathbf{R}$ correspond to process and measurement noise. Their purpose is to achieve a balance between the reliability of the model used for the machine's estimated parameters and the accuracy of the measurement instruments for the current in this case. This is because the current is the only variable that is recorded as observer feedback, even though the speed must also be known to obtain the $\mathbf{A}$ matrix. Thus, this signal is treated as an input.

2.6 Sorting and Greedy Algorithm

The modulation stage allows for synthesizing the reference voltages derived from the current controls for both external and internal tasks. Additionally, it aims to balance the voltages of each submodule within a cluster. Therefore, it is necessary to establish algorithms that simultaneously achieve both objectives.

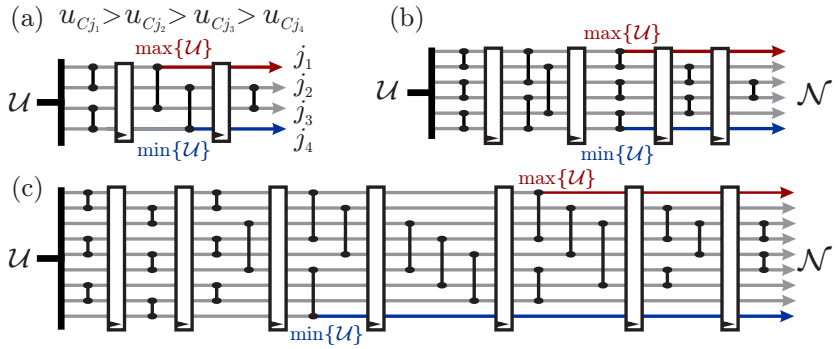

FIGURE 2.6: Sorting with (a) four, (b) six, and (c) nine inputs [3].

Algorithm 1 Greedy Algorithm

Require: $v_\kappa^\star, i_\kappa, \mathcal{N}$, and $\mathcal{U}$

if $i_\kappa > 0$ **then**
  for $j = 1$ to n **do**
    $\mathcal{N}_j = \mathcal{N}_{n-j+1}$; ▷ sorting in increasing order
$m := \text{zeros}(n)$; ▷ all cells starts with $m_j = 0$
$u_\Sigma := 0$;
for $j = 1$ to n **do**
  $\ell := \mathcal{N}_j$;
  if $u_\Sigma + u_{C\ell} \leqslant v_\kappa^\star$ **then**
    $m_\ell := 1$;
    $u_\Sigma := u_\Sigma + u_{C\ell}$;
  else
    $m_\ell := \frac{1}{u_{C\ell}} (v_\kappa^\star + u_\Sigma)$;
    break;
return m;

In this work, the Sorting algorithm will be executed as established in [58] as part of Optimal Sorting Networks. In this algorithm, analysis is performed per cluster, establishing a set $\mathcal{U} = \{u_{C1}, \ldots, u_{Cn}\}$ representing the capacitor voltages and the set $\mathcal{N} = \{j_1, \ldots, j_n\}$ providing the descending order of voltages, meaning u_{Cj_1} is the maximum and u_{Cj_n} the minimum. Thus, the sorting strategy is based on comparison stages between two variables, modifying the output $\mathcal{N}$. Fig. 2.6 illustrates the process for a cluster with four, six, and nine submodules using Knuth notation in [3]. The advantage of this strategy lies in the fact that the number of stages ensuring the order is always fixed and will be of value $n - 1$. Logically, this process can be carried out analogously to sort in ascending order.

Once the set is fully sorted, the Greedy algorithm 1 is then applied by taking the elements of the set $\mathcal{N}$ to synthesize the reference voltage $v_\kappa^\star$ by applying a maximum duty cycle to the first half-bridges, ensuring that only one covers the difference whose value will be:

$$m_\ell = \frac{1}{u_{C\ell}} \left(v_\kappa^\star + \sum_{j=\ell+1}^{n} u_{Cj} - \sum_{j=1}^{\ell-1} u_{Cj} \right) \tag{2.23}$$

From this, it follows that some submodules may not contribute to the modulation if the reference voltage is covered by the other half-bridges. Additionally, the direction of the current must be considered to decide the order in which the groups of semiconductors are activated. When the current is positive, i.e., $i_\kappa > 0$, the set $\mathcal{N}$ should be inverted so that the capacitors with lower voltage are charged to match the value of the others. Similarly, when the current is negative ($i_\kappa < 0$), the capacitors will tend to discharge; therefore, the submodules with higher voltage should modulate to achieve balance.

3. Control Strategy

Behind the control proposal that performs the tasks of cluster balancing and low-frequency oscillation mitigation, a modeling of the cascaded multilevel converters capable of capturing and separating the phenomena for appropriate handling of their variables must be established. Likewise, a cluster energy model must be proposed due to its relevance in the strategy this thesis proposes. This foundation will lead to the optimization problem for the linear COCP, whose application can be varied given the generality of the model and its decoupling from other tasks, however, it is addressed within the context of drives in this work.

3.1 Modelling of Modular Multilevel Cascaded Converters

An important advantage of the proposed control strategy lies in its applicability across all MMCC topologies. However, given the focus of this work, the theory will be specifically presented for the M2C topology. Besides, In this thesis, the overall COCP to deal with the ICB and LFO control tasks are presented first. To do so, let us consider an M2C composed of a set of 6 branches (or edges) $\mathcal{K} = \{1, \dots, 6\}$, a set of $n_1 = 2$ phases (or nodes) at the input-side of the converter and another set of $n_2 = 3$ nodes at the output-side. Then, the branch currents are comprised in the vector $\boldsymbol{i}_\mathrm{s} = \begin{bmatrix} i_1 & \cdots & i_6 \end{bmatrix}^\intercal \in \mathbb{R}^6$ and the input- and output port currents are defined as $\boldsymbol{i}_\mathrm{dc} = [i_\mathrm{P}\, i_\mathrm{N}]^\intercal$ and $\boldsymbol{i}_\mathrm{m}^{abc} = [i_\mathrm{m}^a\, i_\mathrm{m}^b\, i_\mathrm{m}^c]^\intercal$, respectively.

On the one hand, by inspecting the circuit topology in Fig. 3.1, it is possible to establish the following relationship between the branch, and the input- and output-currents:

$$\begin{bmatrix} \boldsymbol{i}_\mathrm{dc} \\ -\boldsymbol{i}_\mathrm{m}^{abc} \end{bmatrix} = \underbrace{\begin{bmatrix} 1 & 1 & 1 & 0 & 0 & 0 \\ 0 & 0 & 0 & 1 & 1 & 1 \\ -1 & 0 & 0 & -1 & 0 & 0 \\ 0 & -1 & 0 & 0 & -1 & 0 \\ 0 & 0 & -1 & 0 & 0 & -1 \end{bmatrix}}_{\mathbf{A}} \boldsymbol{i}_\mathrm{s}. \tag{3.1}$$

Where $\mathbf{A} \in \mathbb{R}^{5\times 6}$ is the incidence matrix of the M2C's directed graph shown in Fig. 3.2.

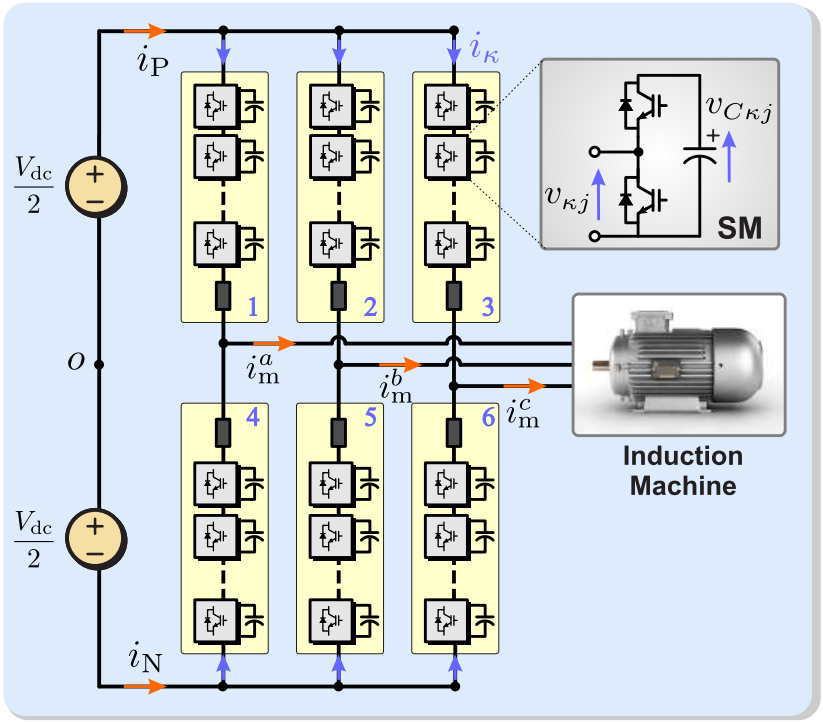

FIGURE 3.1: M2C Topology and drive application.

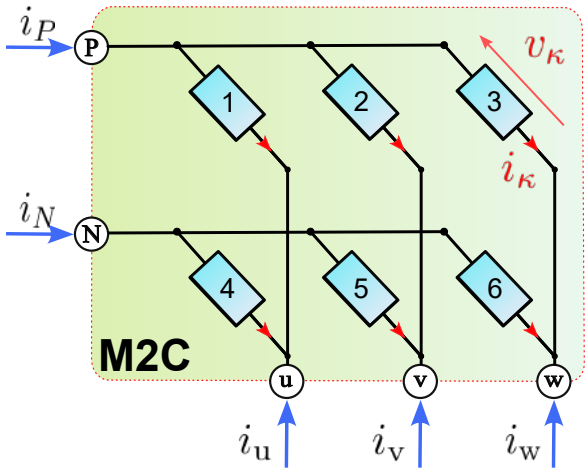

FIGURE 3.2: M2C's directed graph.

The control system proposed in this work injects a circulating current component in each cluster, namely $i_{\kappa z}$ for $\kappa \in \mathcal{K}$, to compensate for possible cluster energy deviations and low-frequency oscillations in the SM-capacitor voltages. These additional branch currents represent the first degrees of freedom to deal with the ICB control and LFO mitigation tasks.

Now, the additional branch currents $i_{\kappa z}$ can be grouped in the following vector:

$$\boldsymbol{i}_z = \begin{bmatrix} i_{1z} & \dots & i_{6z} \end{bmatrix}^{\intercal} \in \mathbb{R}^6 \tag{3.2}$$

It is worth remarking that, the additional branch currents in (3.2) must satisfy the nullspace condition, i.e., $\{\boldsymbol{i}_z \in \mathbb{R}^6 \,|\, \mathbf{A}\boldsymbol{i}_z = 0\}$, to be considered as circulating current components. Therefore, for any injected branch currents $\boldsymbol{i}_z$ satisfying the nullspace condition, the input and output currents are unaffected, achieving a decoupled control of the converter.

Therefore, the branch current vector can be expressed as:

$$\boldsymbol{i}_{\mathrm{s}} = \boldsymbol{i}_{\mathrm{B}} + \boldsymbol{i}_z \tag{3.3}$$

Considering $\boldsymbol{i}_{\mathrm{B}} \in \mathbb{R}^6$ the basic branch current vector. The latter represents the current flowing in the branches when null circulating currents. It only depends on the external port currents. Thus, for a given current in the input- and output-port, the basic branch current vector $\boldsymbol{i}_{\mathrm{B}}$ is determined by using the Moore–Penrose inverse of the incidence matrix as:

$$\boldsymbol{i}_{\mathrm{B}} = \mathbf{A}^{\dagger} \begin{bmatrix} \boldsymbol{i}_{\mathrm{dc}} \\ -\boldsymbol{i}_{\mathrm{m}}^{abc} \end{bmatrix}. \tag{3.4}$$

In this regard, and by considering that the currents fulfill $i_{\mathrm{N}} = -i_{\mathrm{P}}$ at the input-port and $i_{\mathrm{m}}^{a} + i_{\mathrm{m}}^{b} + i_{\mathrm{m}}^{c} = 0$ at the output-port, the basic current vector $\boldsymbol{i}_{\mathrm{B}}$ can be explicitly written as:

$$\boldsymbol{i}_{\mathrm{B}} = \begin{bmatrix} \frac{1}{3} & -\frac{1}{2} & 0 & 0 \\ \frac{1}{3} & 0 & -\frac{1}{2} & 0 \\ \frac{1}{3} & 0 & 0 & -\frac{1}{2} \\ -\frac{1}{3} & -\frac{1}{2} & 0 & 0 \\ -\frac{1}{3} & 0 & -\frac{1}{2} & 0 \\ -\frac{1}{3} & 0 & 0 & -\frac{1}{2} \end{bmatrix} \begin{bmatrix} i_{\mathrm{P}} \\ i_{\mathrm{m}}^{a} \\ i_{\mathrm{m}}^{b} \\ i_{\mathrm{m}}^{c} \end{bmatrix} \tag{3.5}$$

On the other hand, the voltage synthesized by each cluster is

$$v_{\kappa} = \sum_{j \in \mathcal{C}_{\kappa}} u_{\kappa j} v_{C\kappa j}, \qquad \mathcal{C}_{\kappa} = \{1, \ldots, N_{\kappa}\} \tag{3.6}$$

where N_{κ} is the number of SMs in the kth cluster, meanwhile $u_{\kappa j} \in \{0, 1\}$ and $v_{C\kappa j}$ are the switching state and the capacitor voltage of the jth SM. By introducing the cluster voltage vector $\boldsymbol{v}_{\mathrm{s}} = \begin{bmatrix} v_1 & \cdots & v_6 \end{bmatrix}^{\intercal} \in \mathbb{R}^6$, the branch's dynamic model can be expressed as:

$$\mathbf{A}^{\intercal} \begin{bmatrix} \boldsymbol{v}_{\mathrm{dc}} \\ \boldsymbol{v}_{\mathrm{m}}^{abc} \end{bmatrix} = L \frac{\mathrm{d}\boldsymbol{i}_s}{\mathrm{d}t} + R\boldsymbol{i}_s + \boldsymbol{v}_{\mathrm{s}} - \mathbf{1}_{6\times 1} v_0, \tag{3.7}$$

Being $\boldsymbol{v}_{\mathrm{m}}^{abc} = [v_{\mathrm{m}}^{a} \; v_{\mathrm{m}}^{b} \; v_{\mathrm{m}}^{c}]^{\intercal}$ the converter output voltage (respect to the machine neutral), $\boldsymbol{v}_{\mathrm{dc}} = [v_{\mathrm{P}} \; v_{\mathrm{N}}]^{\intercal} = [\frac{V_{\mathrm{dc}}}{2} \; -\frac{V_{\mathrm{dc}}}{2}]^{\intercal}$ the input voltage (respect to the dc-link middle point), and v_0 the voltage between the neutral points. Moreover, L, R are the branch filter parameters.

3.1.1 Decoupling Map

Although the proposed ADMM-based Model Predictive Cluster Energy Control is implemented in the natural framework (abc), the machine control is implemented in a decoupled frame, c.f., [49], to straightforward include the dynamic model of the machine. To this end, and following the M3C's modeling introduced in [80], the linear map $\mathbf{T} : \mathbb{R}^6 \to \mathbb{R}^6$ defined in (3.8) is used

in this work to decouple the control of the input $i_{\mathrm{P}} \in \mathbb{R}$, output $\boldsymbol{i}_m^{\alpha\beta 0} \in \mathbb{R}^3$, circulating $\boldsymbol{i}_\varepsilon \in \mathbb{R}^2$, and zero-sequence current $i_0 \in \mathbb{R}$.

$$\boldsymbol{i}_{\mathrm{s}}' = \begin{bmatrix} i_{\mathrm{P}} \\ \boldsymbol{i}_m^{\alpha\beta 0} \\ \boldsymbol{i}_\varepsilon \end{bmatrix} = \underbrace{\begin{bmatrix} \mathbf{PA} \\ \mathbf{N}^\dagger \end{bmatrix}}_{:=\mathbf{T}} \boldsymbol{i}_{\mathrm{s}} \qquad \Longleftrightarrow \qquad \mathbf{T} := \frac{1}{6}\begin{bmatrix} 3 & 3 & 3 & -3 & -3 & -3 \\ -4 & 2 & 2 & -4 & 2 & 2 \\ 0 & -2\sqrt{3} & 2\sqrt{3} & 0 & -2\sqrt{3} & 2\sqrt{3} \\ 3 & 3 & 3 & 3 & 3 & 3 \\ 1 & -2 & 1 & -1 & 2 & -1 \\ 1 & 1 & -2 & -1 & -1 & 2 \end{bmatrix} \tag{3.8}$$

Where $\mathbf{N} \in \mathbb{R}^{6\times 2}$ is the nullspace matrix of $\mathbf{A}$, which relates the standard circulating currents $\boldsymbol{i}_\varepsilon = [i_{\varepsilon 1}\ i_{\varepsilon 2}]^\intercal$ with the one defined in (3.2) as per $\boldsymbol{i}_z = \mathbf{N}\boldsymbol{i}_\varepsilon$. This matrix is not unique, but in this work the following nullspace matrix is used:

$$\boldsymbol{i}_z = \mathbf{N}\boldsymbol{i}_\varepsilon \quad ; \mathbf{N} = \begin{bmatrix} 1 & 1 \\ -1 & 0 \\ 0 & -1 \\ -1 & -1 \\ 1 & 0 \\ 0 & 1 \end{bmatrix} \qquad \Longrightarrow \qquad \mathbf{N}^\dagger := \frac{1}{6}\begin{bmatrix} 1 & -2 & 1 & -1 & 2 & -1 \\ 1 & 1 & -2 & -1 & -1 & 2 \end{bmatrix} \tag{3.9}$$

Being $\mathbf{N}^\dagger$ the Moore-Penrose inverse of $\mathbf{N}$. Furthermore, in (3.8), matrix $\mathbf{P}$ maps the input and output currents to the $\Sigma\Delta$ and $\alpha\beta 0$ frame, respectively, as:

$$\mathbf{P} = \begin{bmatrix} \mathbf{T}_{\Sigma\Delta} & \mathbf{0}_{2\times 3} \\ \mathbf{0}_{3\times 2} & \mathbf{T}_{\alpha\beta 0} \end{bmatrix} \begin{bmatrix} \boldsymbol{i}_{\mathrm{dc}} \\ -\boldsymbol{i}_{\mathrm{m}}^{abc} \end{bmatrix} \quad ; \mathbf{T}_{\Sigma\Delta} = \frac{1}{2}\begin{bmatrix} 1 & 1 \\ 1 & -1 \end{bmatrix} \quad , \mathbf{T}_{\alpha\beta 0} = \frac{1}{3}\begin{bmatrix} 2 & -1 & -1 \\ 0 & \sqrt{3} & -\sqrt{3} \\ 1 & 1 & 1 \end{bmatrix} \tag{3.10}$$

Therefore, by applying this transformation to (3.7), and considering that the zero-sequence current is zero, i.e., $i_{\mathrm{m}}^0 = 0$, the following decoupled model is obtained:

$$L\frac{\mathrm{d}i_{\mathrm{P}}}{\mathrm{d}t} = -Ri_{\mathrm{P}} + \frac{3}{2}V_{\mathrm{dc}} - v_{\mathrm{sP}} \tag{3.11a}$$

$$L\frac{\mathrm{d}\boldsymbol{i}_{\mathrm{m}}}{\mathrm{d}t} = -R\boldsymbol{i}_{\mathrm{m}} + 2\boldsymbol{v}_{\mathrm{m}} - \boldsymbol{v}_{\mathrm{sm}} \tag{3.11b}$$

$$3v_{\mathrm{m0}} = v_{\mathrm{s0}} - 3v_0 \tag{3.11c}$$

$$L\frac{\mathrm{d}\boldsymbol{i}_\varepsilon}{\mathrm{d}t} = -R\boldsymbol{i}_\varepsilon - \boldsymbol{v}_{\mathrm{s}\varepsilon} \tag{3.11d}$$

Where $\boldsymbol{i}_{\mathrm{m}} = \left[i_{\mathrm{m}}^\alpha\ i_{\mathrm{m}}^\beta\right]^\intercal$ is the stator current, $\boldsymbol{v}_{\mathrm{sm}} = \left[v_{\mathrm{sm}}^\alpha\ v_{\mathrm{sm}}^\beta\right]^\intercal$ is the output cluster voltage in the $\alpha\beta$ frame, and $\boldsymbol{v}_{\mathrm{s}\varepsilon} = \left[v_{\varepsilon 1}\ v_{\varepsilon 2}\right]^\intercal$ is the internal (circulating) cluster voltage. These cluster voltage vectors are determined using $\boldsymbol{v}_{\mathrm{s}}' = \mathbf{T}\boldsymbol{v}_{\mathrm{s}}$.

In order to include the induction machine dynamic model at the output side of the converter, the stator current $\boldsymbol{i}_{\mathrm{m}}^{\alpha\beta}$ and the rotor flux linkage ψ_r in the $\alpha\beta$ frame are selected as state variables. Thus, using the stator current model [81] into (3.11b), the following dynamic model for the output port is obtained:

$$L_{\mathrm{e}}\frac{\mathrm{d}\boldsymbol{i}_{\mathrm{m}}}{\mathrm{d}t} = -R_{\mathrm{e}}\boldsymbol{i}_{\mathrm{m}} + 2\left(\frac{1}{\tau_r}\mathbf{I} - \mathbf{J}\omega\right)k_r\boldsymbol{\psi}_r + \boldsymbol{v}_{\mathrm{sm}} \tag{3.12}$$

With $L_{\mathrm{e}} = L + 2\sigma L_s$ and $R_{\mathrm{e}} = R + 2R_\sigma$ being the equivalent inductance and resistance at the output port, L_s is the stator inductance, $\sigma = 1 - k_r k_s$ is the total leakage coefficient, $k_r = \frac{L_m}{L_r}$ and $k_s = \frac{L_m}{L_s}$ are the magnetic coupling factors, and $R_\sigma = R_s + k_r^2 R_r$. Moreover, $\mathbf{J}$ is the imaginary unity on his matrix form or the rotation matrix. Therefore, the dynamic behavior of the stator current will be mainly determined by the following equivalent time constant:

$$\tau_{\sigma s} = \frac{2\sigma L_s + L}{2R_\sigma + R} \tag{3.13}$$

Besides, from the control point of view, the last term in the left-hand of (3.12) can be considered as a known disturbance. Note that zero-offset is achieved under the assumption that the disturbance and reference dynamics are appropriately included in the prediction model and feasibility of the commanded reference is given [82].

Finally, once the voltages in the transformed framework $\boldsymbol{v}_{sm}$ is obtained, the inverse transformation is carried out to modulate the signals in each cluster and their respective local controller.

3.1.2 Cluster Energy Model

To deal with the ICB control and the LFO mitigation, we will use the cluster energy $E_{C\kappa}$ as the variable to be controlled. From the circuit diagram shown in Fig. 3.1, the κth cluster energy can be expressed as $E_{C\kappa} = \frac{1}{2} C \sum_{j=1}^{N} v_{C\kappa j}^2$, where C is the rated SM's capacitance. Thus, the cluster energy vector, i.e.,

$$\mathbf{E}_C = \begin{bmatrix} E_{C1} & \dots & E_{C6} \end{bmatrix}^{\intercal} \in \mathbb{R}^6, \tag{3.14}$$

is the variable to be controlled.

The dynamic model for $\mathbf{E}_C$ is given by:

$$\mathbf{E}_C = \int_0^t \operatorname{diag}\{\boldsymbol{v}_s\}\, \boldsymbol{i}_s \, \mathrm{d}\tau \tag{3.15}$$

Therefore, by substituting (3.3) and (3.7) in (3.15), neglecting the filter voltage drop, and using Forward Euler, the discrete-time model for the cluster energy vector is:

$$\mathbf{E}_C(k{+}1){=}\mathbf{E}_C(k) + T_s\big[\mathbf{V}_{\mathrm{B}}(k){+}v_0(k)\mathbf{I}_6\big]\big(\boldsymbol{i}_{\mathrm{B}}(k){+}\boldsymbol{i}_z(k)\big), \tag{3.16}$$

Where $\mathbf{V}_{\mathrm{B}}(k)$ is a diagonal matrix depending on the external voltages at instant k, i.e.,

$$\mathbf{V}_{\mathrm{B}}(k) = \operatorname{diag}\left\{ \mathbf{A}^{\intercal} \begin{bmatrix} \boldsymbol{v}_{\mathrm{dc}}(k) \\ \boldsymbol{v}_{\mathrm{m}}^{abc}(k) \end{bmatrix} \right\} \in \mathbb{R}^{6\times 6} \tag{3.17}$$

The energy model shown in (3.16) represents a time-varying nonlinear system in which the circulating currents $\boldsymbol{i}_z$ and the common-mode voltage v_0 can be considered the control actions, giving a highly coupled dynamical system which entails significant control complexity. However, to simplify the control problem, most of the control algorithms presented in the literature assume that the CMV to be injected $v_0^\star$ is a known variable [31, 25, 83]. In this regard, a high-frequency signal is preferred to avoid extra low-frequency components in the cluster power [49]. As a result, the discrete-time model in (3.16) becomes linear with respect to the circulating currents, as follows:

$$\mathbf{E}_C(k{+}1) = \mathbf{E}_C(k) + \mathbf{B}(k)\boldsymbol{i}_z(k) + \boldsymbol{d}(k) \tag{3.18}$$

Where the input matrix is defined as:

$$\mathbf{B}(k) = T_s\big(\mathbf{V}_{\mathrm{B}}(k) + v_0(k)^*\mathbf{I}_6\big) \in \mathbb{R}^{6\times 6} \tag{3.19}$$

and $\boldsymbol{d}(k) = \mathbf{B}(k)\boldsymbol{i}_{\mathrm{B}}(k)$ is a known disturbance.

3.2 The proposed ADMM-based MPC strategy

The control system requires performing the control of the internal cluster variables, that is, branch current i_κ, SM capacitor voltages $v_{C\kappa j}$, and the energy in every cluster $E_{C\kappa}$. The latter will be the variable to be controlled by the proposed control strategy.

The overall control structure of the converter is depicted in Fig. 3.3. The grey blocks represent conventional control loops like Field-Oriented Control for the machine side (AC-port) and TEB Control. The emphasis of this document is placed on the reference generation stage for the circulating currents within a natural framework. To compute these signal references, the proposed Cluster Energy Control (CEC) takes as input data the current references ($\boldsymbol{i}^*_{\mathrm{m}}$ and i^*_{P}) from the aforementioned external controls, in addition to the energy cluster vector $\mathbf{E}_C$, the dc-link voltage $\mathrm{V_{dc}}$ and an arbitrary signal for the CMV.

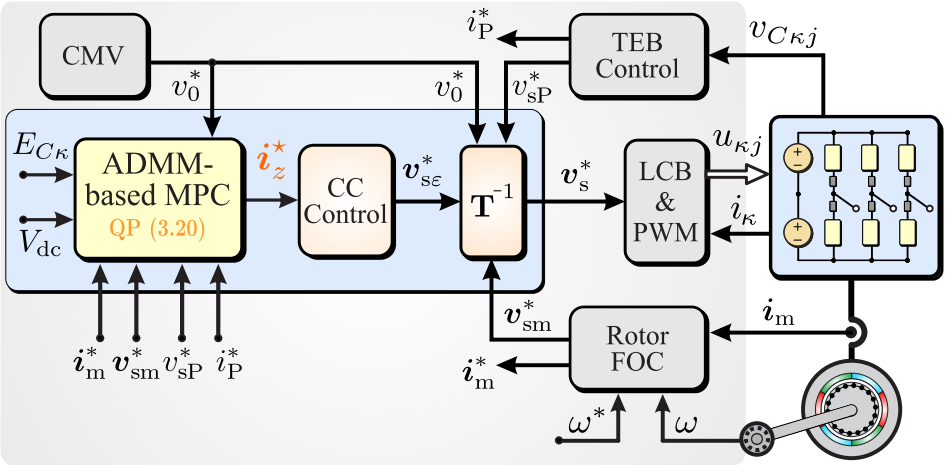

FIGURE 3.3: Overall control scheme for the M2C. The ADMM-based MPC is detailed in section 3.2.2.

3.2.1 MPC Formulation for the Cluster Energy Control

To obtain the optimal circulating currents $\boldsymbol{i}_z$, the following constrained optimal control problem (COCP) for reference tracking of the cluster energy vector $\mathbf{E}_C$ over the prediction horizon $\mathcal{H} = \{0, 1, \ldots, N_p - 1\}$, is proposed in this work:

$$\min_{\boldsymbol{i}_z(\ell)} \quad J = \sum_{\ell\in\mathcal{H}} \big\|\mathbf{E}_C(\ell+1) - \mathbf{E}_C^*\big\|^2_{\boldsymbol{Q}} + \lambda_z \big\|\boldsymbol{i}_z(\ell)\big\|_2^2 \tag{3.20a}$$

$$\text{s.t.} \quad \mathbf{E}_C(\ell+1) = \mathbf{E}_C(\ell) + \boldsymbol{d}(\ell) + \mathbf{B}(\ell)\boldsymbol{i}_z(\ell) \tag{3.20b}$$

$$\mathbf{A}\boldsymbol{i}_z(\ell) = \mathbf{0} \tag{3.20c}$$

$$\boldsymbol{I}_{\mathrm{L}}(k) \leqslant \boldsymbol{i}_z(k) \leqslant \boldsymbol{I}_{\mathrm{U}}(k)\,, \quad \forall \ell \in \mathcal{H} \tag{3.20d}$$

The quadratic cost function presented in (3.20a) penalizes the predicted tracking error weighted by the diagonal matrix $\boldsymbol{Q} = \text{diag}\{q_1, \cdots, q_6\}$. Additionally, the weighting factor $\lambda_z > 0$ is a tuning parameter that adjusts the trade-off between the tracking accuracy and the control effort. The latter is proportional to the power losses generated by the circulating currents and must be reduced as much as possible.

In the COCP presented in (3.20), the decision variables are the additional branch currents $\boldsymbol{i}_z$ (or circulating currents) over the finite horizon $\mathcal{H}$, leading to a quadratic programming (QP) problem of size $6N_p$. Thus, the controller aims to minimize the cost function (3.20a) over the circulating currents that satisfy the inequality constraints regarding the upper and lower bounds for the circulating currents given in (3.20d). These limits are time-varying since they depend on the input and output current references, $i_{\text{P}}^{\star}$ and $\boldsymbol{i}_{\text{m}}^{\star}$, respectively. The upper and lower limits for the cluster currents can be deduced from (3.3) as:

$$\begin{cases} \boldsymbol{I}_{\text{U}}(k) & = I_{\max}\mathbf{1}_6 - \boldsymbol{i}_{\text{B}}^{\star}(k) \\ \boldsymbol{I}_{\text{L}}(k) & = -I_{\max}\mathbf{1}_6 - \boldsymbol{i}_{\text{B}}^{\star}(k). \end{cases} \tag{3.21}$$

Being $I_{\max}$ the rated branch over-current limit, and $\boldsymbol{i}_{\text{B}}^{\star}$ is determined by using (3.4).

It is worth to emphasize that in this work, to inject circulating currents, the nullspace condition (3.20c) is explicitly included in the COCP to guarantee that the circulating currents in $\boldsymbol{i}_z(k)$ neither affect the input nor the output currents.

3.2.2 Reformulation of the Original Constrained Optimal Control Problem to apply the ADMM method.

Regardless of the MMC topology, the number of variables that the problem needs to solve increases with prediction horizon, leading to heightened complexity in real-time solution. Therefore, the ADMM algorithm is introduced to address this issue while simultaneously achieving an extended prediction horizon. As emphasized in [84], the philosophy of ADMM is a decomposition-coordination procedure in which the solutions to small local sub-problems are coordinated to find a solution to a large-scale global problem. However, ADMM is not directly applicable to problem (3.23) since its cost function includes more than 2 blocks without coupled variables in the optimization problem. The above can be resolved by transforming the original multiblock problem into an equivalent two-block one by introducing splitting variables and indicator functions [85] although this approach substantially increases the number of variables and constraints in the problem, limiting its implementation on real-time embedded systems.

Moreover, The circulating currents of the QP problem presented in (3.20) must satisfy the bounds constraint and the nullspace condition along the prediction horizon. Since the incidence matrix $\mathbf{A}$ is not full-rank, finding an efficient QP solver for solving (3.20) is not straightforward. However, the ADMM algorithm proposed in this work guarantees the convergence of the problem without relying on assumptions about this matrix $\mathbf{A}$, meaning it is not necessary for the matrix to fulfil the full rank condition [38], making it a suitable method for the present application.

To apply the ADMM algorithm, the circulating current in the κth cluster over the prediction horizon is introduced:

$$\boldsymbol{z}_{\kappa} = [i_{z\kappa}(0)\ i_{z\kappa}(1)\ \cdots\ i_{z\kappa}(N_p-1)]^{\intercal} \in \mathbb{R}^{N_p}, \tag{3.22}$$

By using every control sequence introduced in (3.22), the QP stated in (3.20) can be rewritten as the following separable optimization problem:

$$\min_{\boldsymbol{z}_\kappa} \quad J = \sum_{\kappa\in\mathcal{K}} J_\kappa\left(E_{C\kappa}(0), \boldsymbol{z}_\kappa\right) \tag{3.23a}$$

$$\text{s.t.} \quad \sum_{\kappa\in\mathcal{K}} \mathbf{A}_\kappa \boldsymbol{z}_\kappa = 0 \tag{3.23b}$$

$$\boldsymbol{z}_\kappa \in \mathcal{B}_\kappa, \qquad \forall \kappa \in \mathcal{K} = \{1, \ldots, 6\} \tag{3.23c}$$

where $J_\kappa : \mathbb{R}^{N_p} \mapsto \mathbb{R}_+$ is the compact quadratic cost function associated to the κth cluster. It is given by:

$$J_\kappa = \boldsymbol{z}_\kappa^\intercal \mathbf{H}_\kappa \boldsymbol{z}_\kappa + 2\boldsymbol{z}_\kappa^\intercal \boldsymbol{f}_\kappa + \nu(E_C(0)), \tag{3.24}$$

considering:

$$\mathbf{H}_\kappa = \mathbf{B}_\kappa^\intercal q_\kappa \mathbf{B}_\kappa + \lambda_z \mathbf{I}_{N_p} \tag{3.25}$$

$$\boldsymbol{f}_\kappa = \mathbf{B}_\kappa^\intercal q_\kappa (\mathbf{1}_{N_p}(E_{C\kappa}(0) - E_{C\kappa}^*) + \mathbf{D}\boldsymbol{d}_\kappa) \tag{3.26}$$

Where matrices $\mathbf{B}_\kappa \in \mathbb{R}^{N_p \times N_p}$ and $\boldsymbol{d}_\kappa \in \mathbb{R}^{N_p \times 1}$ are obtained from the predicted trajectory of the κth cluster energy:

$$\underbrace{\begin{bmatrix} E_{C\kappa}(1) \\ E_{C\kappa}(2) \\ \vdots \\ E_{C\kappa}(N_p) \end{bmatrix}}_{:=\boldsymbol{E}_{C\kappa}} = \underbrace{\begin{bmatrix} 1 \\ 1 \\ \vdots \\ 1 \end{bmatrix}}_{\mathbf{1}_{N_p}} E_{C\kappa}(0) + \underbrace{\begin{bmatrix} 1 & 0 & 0 & \cdots & 0 \\ 1 & 1 & 0 & \cdots & 0 \\ \vdots & \vdots & \ddots & \ddots & \vdots \\ 1 & 1 & 1 & \cdots & 1 \end{bmatrix}}_{:=\mathbf{D}} \boldsymbol{d}_\kappa + \mathbf{B}_\kappa \underbrace{\begin{bmatrix} i_{\kappa z}(0) \\ i_{\kappa z}(1) \\ \vdots \\ i_{\kappa z}(N_p{-}1) \end{bmatrix}}_{:=\boldsymbol{z}_\kappa} \tag{3.27}$$

With:

$$\mathbf{B}_\kappa = \begin{bmatrix} b_\kappa(0) & 0 & 0 & \cdots & 0 \\ b_\kappa(0) & b_\kappa(1) & 0 & \cdots & 0 \\ \vdots & \vdots & \ddots & \ddots & \vdots \\ b_\kappa(0) & b_\kappa(1) & b_\kappa(2) & \cdots & b_\kappa(N_p{-}1) \end{bmatrix} \tag{3.28}$$

$$\boldsymbol{d}_\kappa = \begin{bmatrix} d_\kappa(0) \\ d_\kappa(1) \\ \vdots \\ d_\kappa(N_p{-}1) \end{bmatrix} \tag{3.29}$$

In addition, the set $\mathcal{B}_\kappa \subseteq \mathbb{R}^{N_p}$ is the box derived from constraint (3.20d).

On the other hand, in the separable optimization problem presented in (3.23), $\mathbf{A}_\kappa$ is a block diagonal matrix defined as:

$$\mathbf{A}_\kappa = \text{diag}\{\boldsymbol{a}_\kappa, \cdots, \boldsymbol{a}_\kappa\} \in \mathbb{R}^{5N_p \times N_p} \tag{3.30}$$

where $\boldsymbol{a}_\kappa \in \mathbb{R}^5$ is the κth column vector of the incidence matrix $\mathbf{A} = \begin{bmatrix} \boldsymbol{a}_1 \, \boldsymbol{a}_2 \cdots \boldsymbol{a}_6 \end{bmatrix}^\intercal$ given in (3.1).

Motivated by the philosophy of ADMM, an Extended ADMM algorithm is introduced in [75], yielding to the sequential (or alternating) update scheme presented as follows:

$$\boldsymbol{z}_1^{(i+1)} = \arg\min_{\boldsymbol{z}_1 \in \mathcal{B}_1} \mathcal{L}_\rho\big(\boldsymbol{z}_1, \boldsymbol{z}_2^{(i)}, \ldots, \boldsymbol{z}_6^{(i)}, \lambda^{(i)}\big) \tag{3.31a}$$

$$\boldsymbol{z}_2^{(i+1)} = \arg\min_{\boldsymbol{z}_2 \in \mathcal{B}_2} \mathcal{L}_\rho\big(\boldsymbol{z}_1^{(i+1)}, \boldsymbol{z}_2, \ldots, \boldsymbol{z}_6^{(i)}, \lambda^{(i)}\big) \tag{3.31b}$$

$$\vdots \quad \vdots$$

$$\boldsymbol{z}_6^{(i+1)} = \arg\min_{\boldsymbol{z}_6 \in \mathcal{B}_6} \mathcal{L}_\rho\big(\boldsymbol{z}_1^{(i+1)}, \boldsymbol{z}_2^{(i+1)}, \ldots, \boldsymbol{z}_6, \lambda^{(i)}\big) \tag{3.31c}$$

$$\lambda^{(i+1)} = \lambda^{(i)} - \rho \sum_{\kappa \in \mathcal{K}} \mathbf{A}_\kappa \boldsymbol{z}_\kappa^{(i+1)} \tag{3.31d}$$

In (3.31), i represents the iteration counter, $\lambda \in \mathbb{R}^{5N_p}$ is the Lagrangian multiplier (dual variable), $\rho > 0$ is a parameter used to penalise the violation of the linear constraint (nullspace condition), and $\mathcal{L}_\rho(\cdot)$ denotes the augmented Lagrangian of (3.23), which is defined as:

$$\mathcal{L}_\rho(\boldsymbol{z}_\kappa, \lambda) = \sum_{\kappa \in \mathcal{K}} \big(J_\kappa(\boldsymbol{z}_\kappa) - \lambda^\intercal \mathbf{A}_\kappa \boldsymbol{z}_\kappa\big) + \frac{\rho}{2} \Big\| \sum_{\kappa \in \mathcal{K}} \mathbf{A}_\kappa \boldsymbol{z}_\kappa \Big\|_2^2 \tag{3.32}$$

The algorithm presented in (3.31) is straightforward, consisting of a sequential optimization of the circulating currents $\boldsymbol{z}_\kappa$ (primal variables) followed by a dual variable update as shown in (3.31d). In each iteration, the augmented Lagrangian (3.32) is minimized over only one circulating current since the others are considered fixed. Thus, each update of the circulating current involves solving a QP problem of size N_p with upper and lower bounds given by the box set $\mathcal{B}_\kappa$. To efficiently solve these QPs, various iterative algorithms have been proposed in the literature [86]. In particular, active-set methods have been shown to effectively obtain the optimal solution in each iteration for small- and medium-sized problems. To do so, the augmented Lagrangian in (3.32) is rewritten in the standard quadratic form:

$$\mathcal{L}_\rho(\boldsymbol{z}_\kappa, \lambda) = \boldsymbol{z}_\kappa^\intercal \mathbf{H}_{\rho\kappa} \boldsymbol{z}_\kappa + 2\boldsymbol{z}_\kappa^\intercal \boldsymbol{f}_{\rho\kappa} + \nu(E_C(0)) \tag{3.33}$$

where:

$$\begin{aligned} \mathbf{H}_{\rho\kappa} &= \mathbf{B}_\kappa^\intercal q_\kappa \mathbf{B}_\kappa + \mathbf{I}_{N_p} \lambda_z + \rho \mathbf{I}_{N_p} \\ \boldsymbol{f}_{\rho\kappa} &= \mathbf{B}_\kappa^\intercal q_\kappa (\mathbf{1}_{N_p}(E_{C\kappa}(0) - \mathbf{1}_{N_p} E_{C\kappa}^*) + \mathbf{D}\boldsymbol{d}_\kappa) - \lambda^\intercal \mathbf{A}_\kappa + \rho \mathbf{C}_\kappa^\intercal \end{aligned} \tag{3.34a}$$

The matrix $\mathbf{C}_\kappa \in \mathbb{R}^{1 \times N_p}$ is derived from the development of the null space condition provided by the last term of (3.32), denoting the coupling between the primal variables and it is defined as follows:

$$\mathbf{C} = \begin{bmatrix} \mathbf{C}_1 \\ \mathbf{C}_2 \\ \mathbf{C}_3 \\ \mathbf{C}_4 \\ \mathbf{C}_5 \\ \mathbf{C}_6 \end{bmatrix} = \begin{bmatrix} \boldsymbol{z}_2 + \boldsymbol{z}_3 + \boldsymbol{z}_4 \\ \boldsymbol{z}_1 + \boldsymbol{z}_3 + \boldsymbol{z}_5 \\ \boldsymbol{z}_1 + \boldsymbol{z}_2 + \boldsymbol{z}_6 \\ \boldsymbol{z}_1 + \boldsymbol{z}_5 + \boldsymbol{z}_6 \\ \boldsymbol{z}_2 + \boldsymbol{z}_4 + \boldsymbol{z}_6 \\ \boldsymbol{z}_3 + \boldsymbol{z}_4 + \boldsymbol{z}_5 \end{bmatrix} \tag{3.35}$$

Finally, based on the principle of receding horizon control, only the first element of each optimal sequence in (3.22) defines the optimal circulating currents to be injected in the converter:

$$\boldsymbol{i}_z^\star = [i_{z1}^\star(0)\ i_{z2}^\star(0)\ \cdots\ i_{z6}^\star(0)]^\intercal \in \mathbb{R}^6 \tag{3.36}$$

One of the main features of this algorithm is that it converges to the globally optimal solution when all the functions J_κ are strongly convex [76, 77]. This condition is fulfilled in (3.23) since the Hessian matrix $\mathbf{H}_\kappa$, associated with each cluster cost function in (3.24), is positive definite for all $\kappa \in \mathcal{K}$.

3.3 Inner MPC for Branch Current Control

The online reference generation relies on a current controller, whose control strategy necessitates resorting to the general model given by equation (3.7). It is essential to note that the circulating current components, denoted as $\boldsymbol{z}_\kappa$, generated through the ADMM algorithm do not limit the primal variables to any frequency spectrum. Therefore, it is crucial for the local controllers to have a broad bandwidth, which is achieved with Continuous Control Set Model Predictive Control (CCS-MPC), directly applicable in the natural framework (abc) or a decoupled framework as is the case here.

3.3.1 CCS-MPC for Circulating Current

To effectively control the circulating current references provided by the proposed ADMM-based MPEC, a CCS-MPC is implemented in this work. To do so, the following discrete-time model is obtained from (3.11d):

$$\boldsymbol{i}_\varepsilon(k+1) = \mathbf{F}\boldsymbol{i}_\varepsilon(k) + \mathbf{G}\boldsymbol{v}_{\mathrm{s}\varepsilon}(k) \tag{3.37}$$

where $\mathbf{F} = \mathrm{e}^{-\frac{T_s R}{L}}\mathbf{I}_2$ and $\mathbf{G} = \frac{1}{R}(\mathrm{e}^{-\frac{T_s R}{L}} - 1)\mathbf{I}_2$. Taking the above into consideration, the COCP underlying the CC control is formulated as:

$$\min_{\boldsymbol{v}_{s\varepsilon}} \quad \left\|\boldsymbol{i}_\varepsilon(k+1) - \boldsymbol{i}_\varepsilon^*(k)\right\|_2^2 + \lambda_u \left\|\boldsymbol{v}_{\mathrm{s}\varepsilon}(k) - \boldsymbol{v}_{\mathrm{s}\varepsilon}^*(k)\right\|_2^2 \tag{3.38a}$$

$$\text{s.t.} \quad \boldsymbol{i}_\varepsilon(k+1) = \mathbf{F}\boldsymbol{i}_\varepsilon(k) + \mathbf{G}\boldsymbol{v}_{\mathrm{s}\varepsilon}(k) \tag{3.38b}$$

$$\boldsymbol{v}_{\mathrm{s}\varepsilon} \in \mathcal{V} \tag{3.38c}$$

where λ_u weighs the control effort over the tracking error. The circulating current reference in the transformed space is computed as $\boldsymbol{i}_\varepsilon^* = \mathbf{T}_z \boldsymbol{i}_z^\star$, where $\mathbf{T}_z$ denotes the last two rows of matrix $\mathbf{T}$ presented in (3.8). Finally, the set $\mathcal{V}$ represents the feasible region for the circulating cluster voltages.

4. Experimental Setup Testing

With all the proposed and previously described theory, we proceed to the validation phase of the energy control introduced in this thesis, which will be carried out through experimentation with a reduced prototype. The tests will be typical for an electric drive, considering both motor startup and steady-state operation under the conditions of interest established in the objectives, and also evaluating the performance of the ADMM algorithm at each moment.

4.1 Testing Setup

The proposed control system was experimentally validated on the experimental setup shown in Fig. 4.1. This setup comprises an M2C of 4 SMs per cluster driving an induction machine, as shown in Table 4.1. To provide a mechanical load on the shaft, another induction machine is coupled mechanically. The DC port is connected to a programmable unidirectional DC voltage source (KEYSIGHT N8742A).

The system was controlled using the OPAL-RT OP4510 and OP4520 platforms, equipped with a QuadCore 3.3 GHz processor and a Xilinx KINTEX-7 FPGA. The platform executes the control scheme using a sampling time of 167 μs for all involved algorithms. An incremental encoder of 4096 PPR was used to determine the speed, and cluster currents and capacitor voltages were obtained through Hall effect transducers. Moreover, a third harmonic CMV was injected during the tests, whose amplitude decreases as the stator frequency ω_s increases [31], i.e.,:

$$v_0(t) = 0.8\frac{V_{\text{cmv}}}{2}\left(1 - \frac{\omega_s}{\omega_{sN}}\right)\sin\left(3\omega_s t\right) \tag{4.1}$$

where $V_{\text{cmv}} = 500$ V, and ω_{sN} is the nominal stator frequency. Thus, the CMV leads the converter to greater modulation indexes, especially at low speeds up to around 10 Hz. Additionally, constraint in (3.38c) was treated as a box constraint set at 100 V.

FIGURE 4.1: Experimental setup composed of the MMC (M2C) converter, DC current source, and induction machines coupled together.

TABLE 4.1: M2C and Induction Machine Parameters for experimental results.

Parameter	Value
DC-Link Input voltage, V_{dc}	520 V
SM's Nominal DC voltage, V_{C}	130 V
SMs per clusters, N	4
SM capacitance, C	987 μF
PWM Frequency, f_{cr}	6 kHz
Cluster filter parameters, R, L	0.1 Ω, 5 mH
Rated Machine Voltage, V_m	380 V
Power, P	3 kW
Rated Speed, n	1450 rpm
Frequency, f	50 Hz
Pair poles, p	2
Stator/Rotor resistances, R_s/R_r	1.8/1.8 Ω
Stator/Rotor leakage inductances, $L_{\sigma s}/L_{\sigma r}$	2.6/2.6 mH
Mutual inductance, L_m	235 mH

4.1.1 Transient Performance

The performance of the proposed control algorithm was dynamically validated by accelerating the system from a standstill to 800 rpm under a mechanical load of 60% of its rated value, followed by braking back to a standstill. The weighting factors are adjusted to achieve similar circulating currents during these tests.

Additionally, two performance indexes were used to demonstrate the impact of extending the horizon prediction on the M2C performance: (i) the RMS average value of circulating currents normalized by the RMS basic currents defined in (3.4) considering T_o/T_s samples; and

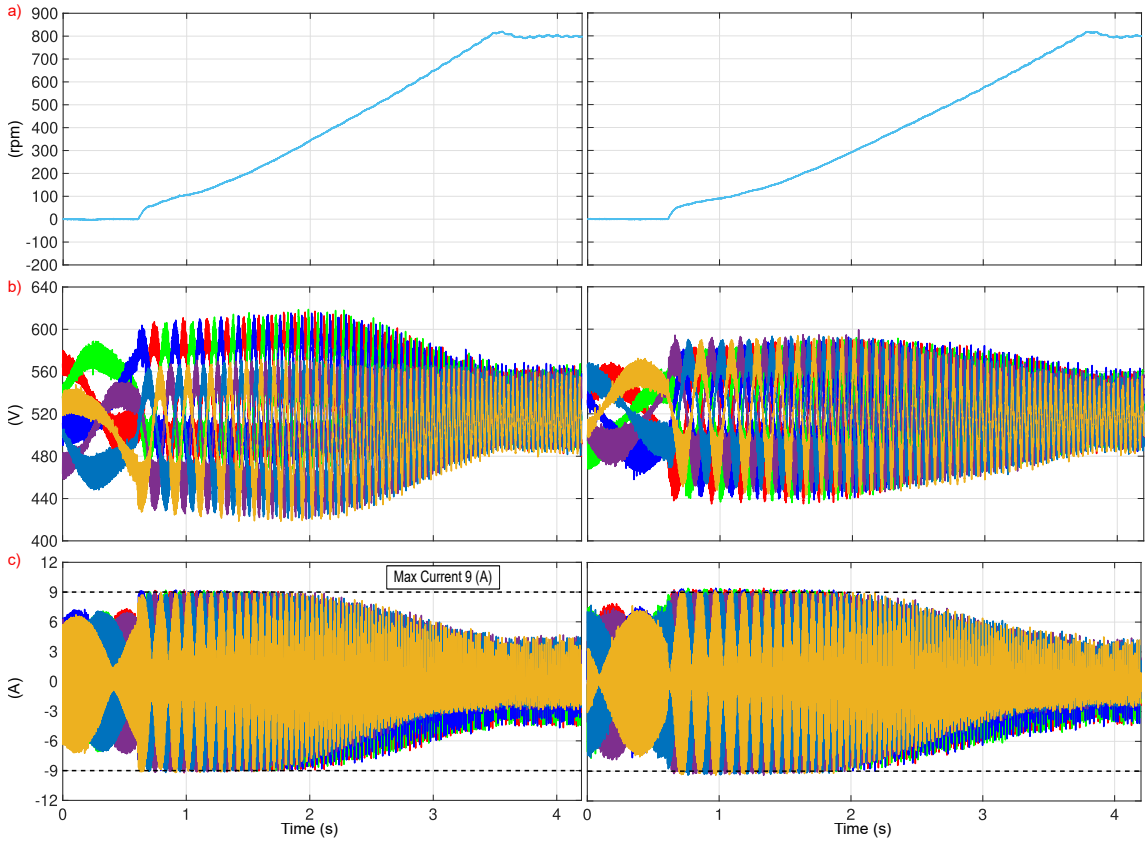

FIGURE 4.2: Experimental results under machine start-up with prediction horizon $N_p = 1$ (Column 1) and $N_p = 6$ (Column 2): (a) Rotor Speed (b) Cluster Capacitor Voltage (c) Circulating Currents.

(ii) the standard deviation of the cluster voltages respected to its desired average value v_C^*. They are defined respectively as:

$$\bar{I}_{cc} = \frac{1}{6}\sum_{\kappa=1}^{6}\frac{I_{z\kappa}}{I_{B\kappa}} \tag{4.2}$$

$$\Delta V_\kappa = 100\,\frac{T_s}{T_o}\sum_{k\in\mathcal{S}}\frac{1}{v_C^*}\sqrt{\frac{\sum_{j=1}^{4}(v_C^* - v_{C_j}(k))^2}{4}} \tag{4.3}$$

where T_o is a time interval to cover at least one cycle of the signal, and $\mathcal{S} = \{1, \ldots, T_o/T_s\}$. Since this calculation is for each cluster, the final indicator is the average value, i.e., $\Delta\bar{V} = \frac{1}{6}\sum_{\kappa=1}^{6}\Delta V_\kappa$. This performance index is related to the first term in the cost function presented in (3.20a) and $\bar{I}_{cc}$ with the control effort.

Fig. 4.2 shows the dynamic performance of the startup for $N_p = 1$ and $N_p = 6$ with weighting factors λ_z of 0.023 and 0.1, respectively. As shown in Fig. 4.2(b)-(c), during the initial moments, the machine startup requires saturated circulating currents in the M2C to balance and compensate for low-frequency oscillations in the capacitor voltages. However, for

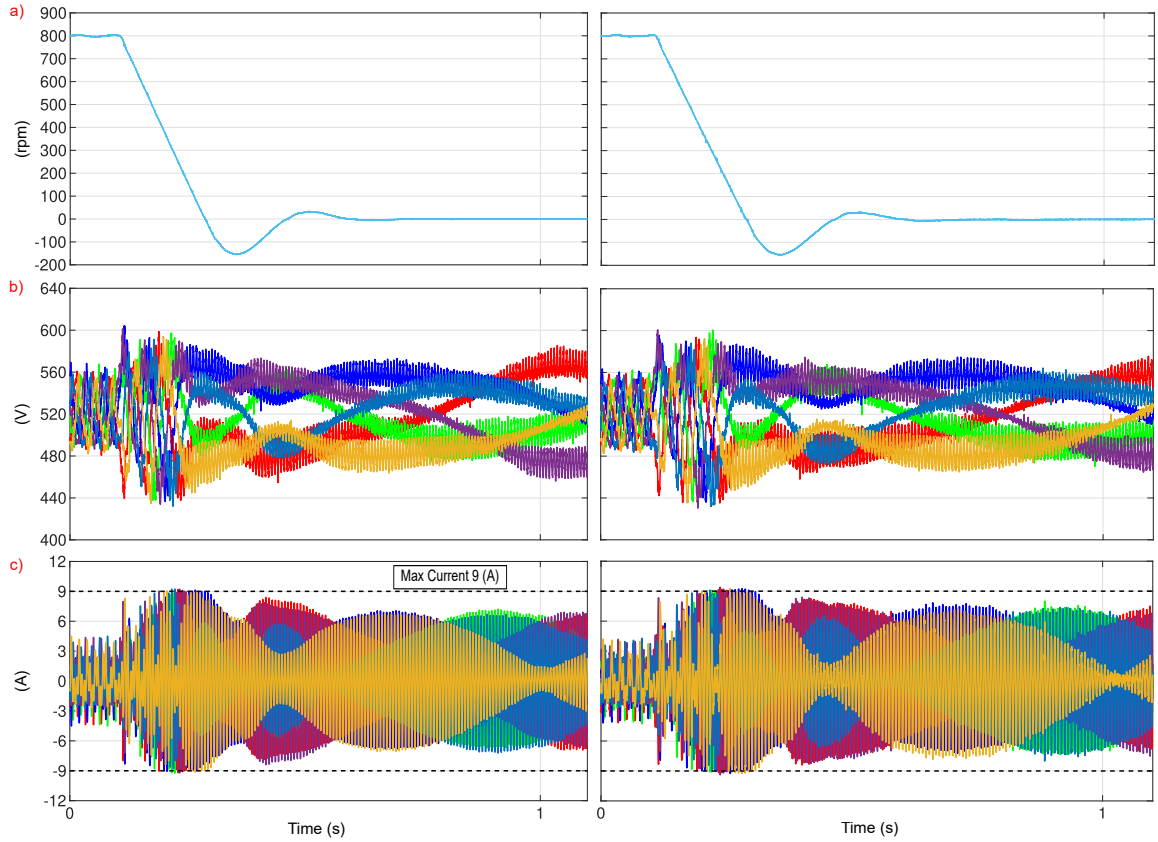

FIGURE 4.3: Experimental results under machine braking with prediction horizon $N_p = 1$ (Column 1) and $N_p = 6$ (Column 2): (a) Rotor Speed (b) Cluster Capacitor Voltage (c) Circulating Currents.

extended horizon case, the peak value of the capacitor voltages was significantly reduced from 620 V to 590 V.

Additionally, the closed-loop performance during braking from 800 rpm is depicted in Fig. 4.3. For both prediction horizons, the constraint in (3.20d) remains active, demonstrating that the proposed control algorithm effectively ensures the safe operation of the M2C by maintaining the circulating currents within their prescribed limits. During braking, the capacitor voltage oscillations are comparable across both horizons; however, the extended prediction horizon achieves a lower voltage ripple at zero speed.

On the other hand, the Common-Mode voltage being an additional input causes a change in the circulating currents, whose frequency spectrum is obtained by using Fourier Decomposition and illustrated in Fig. 4.4 for six different stationary operations considering a fixed tuning on λ_z and N_p. Therefore, the spectrum is mainly composed of $f_{\text{cmv}} \pm f_e$ and $2f_e$ components which demonstrates the influence of both the output port frequency and the frequency chosen for the common mode voltage injection. This frequency component in the current helps to cancel out the power components coming from the arbitrary CMV signal. It is also clear that the components involving the frequency coming from common-mode injection decrease

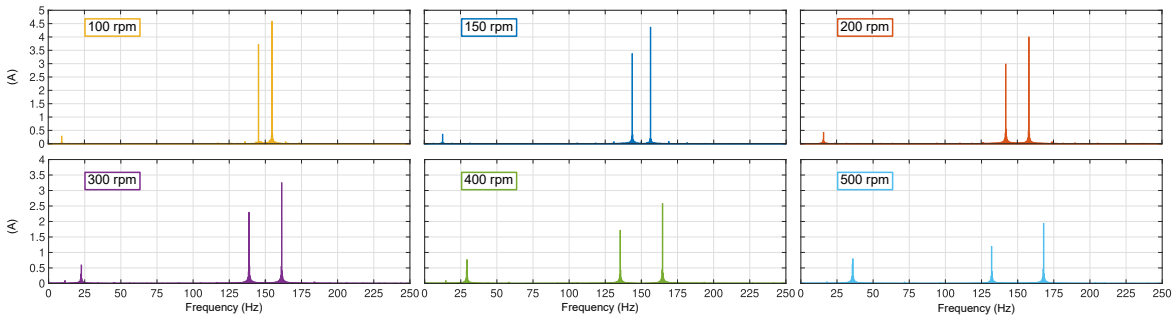

FIGURE 4.4: Frequency spectrum of the circulating current in cluster 1 at steady state considering $N_p = 1$ and $\lambda_z = 0.04$.

in amplitude as the speed increases, being consistent with the CMV reduction. Although the $2f_e$ component varies slightly across speeds, it increases with higher speeds since the applied torque remains constant.

That said, considering some horizons, the indicators of interest were obtained as signals over time during the startup dynamics, considering a high-demand case with low weight factors and a more relaxed case reflected in the amount of required current. Thus, Fig. 4.5 shows for both cases the validation of what was proposed and previously mentioned in the dynamic test. The most relaxed case shown in Fig. 4.5a)-b), ratifies that the extended horizon improves the performance using circulating currents similar to the case with $N_p = 1$, depending on the weight factor election since the prediction horizon $N_p = 6$ reduces the oscillations more than the case with $N_p = 5$ but using larger current values even slightly exceeding the base case in some moments. For $N_p = 3$ the weight factor causes a operation more undesirable than the previous ones due to worse performance at the beginning. Likewise, representing the demanding case in 4.5c)-d) the prediction step $N_p = 5$ achieves the most significant reduction in oscillations compared to the base case $N_p = 1$, lowering the standard deviation by 1% at its peak, achieving a reduction of about 2% of the oscillations amplitude with a current of the same value. For the cases of $N_p = 3$ and $N_p = 6$, although the reduction is smaller, it is observed that operation with less current is achieved, implying a gain in control efficiency. However, for the most demanding case, the current at start-up is always higher when the horizon extends to more than one. In any case, the subsequent reduction makes a decrease in losses as a start-up maneuver.

In both illustrated cases, it is observed that the performance demands currents that, in many instances, exceed the value imposed by the controls performing external tasks when it comes to a critical point for the matrix converter (low frequency high torque), i.e., $I_{z\kappa} \geqslant I_{B\kappa}$. This implies operating with losses around twice the expected amount. Although it is possible to reduce the required current as observed, there will be a tradeoff with the maximum acceptable voltage oscillations for the operation, which falls outside the specific objective of this work but is considered to protect the integrity of the converter.

It is important to highlight the shape in Fig. 4.5d), where the behaviour of the indicator differs from the others between 1.5 s $<$ t $<$ 2.5 s, this effect is studied using Fig. 4.2b) in his first column which exposes that the voltage oscillations not only increase in magnitude, but also deviate from the mean value during the time mentioned and this caused mainly by two factors: first, the small weight factor requesting more current, and second, the interaction between this

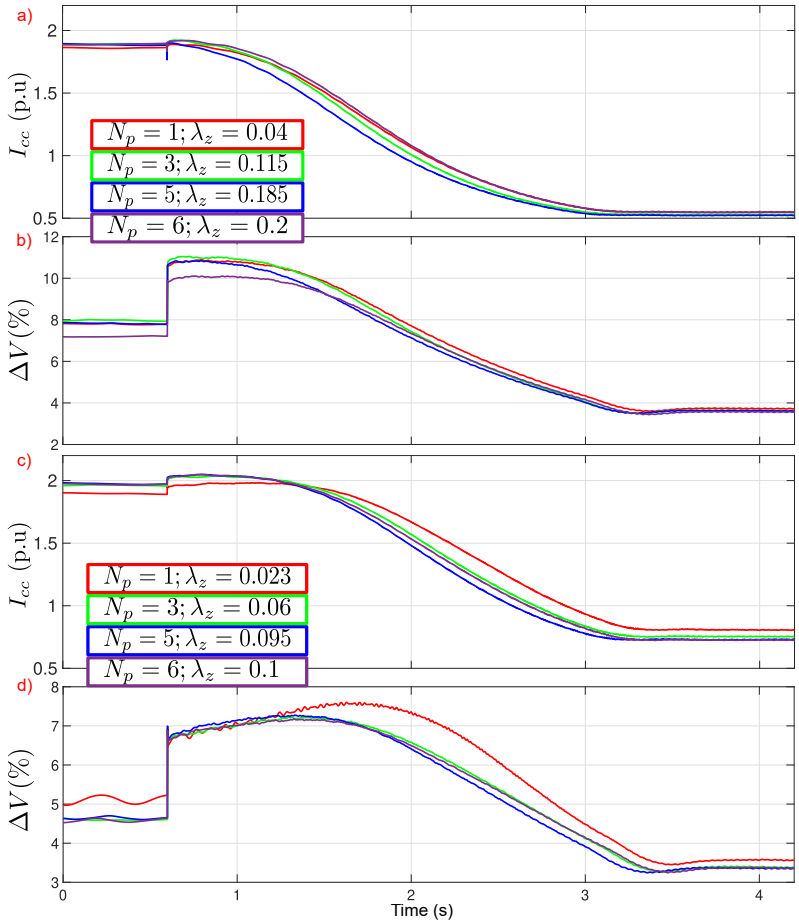

FIGURE 4.5: Experimental results under machine startup with different prediction horizon and fixed weight factor λ_z in each N_p. Two cases are illustrated, taking as base case $N_p = 1, \lambda_z = 0.04$ (rows 1-2) and $N_p = 1, \lambda_z = 0.023$ (rows 3-4): (a)-(c) Circulating Currents mean RMS (b)-(d) Cluster Voltage Standard Deviation.

variable and the common-mode voltage generating an energy component that typically has a near-zero value but grows in magnitude. This component denotes the deviation between upper and lower clusters, therefore, a non-zero value implies the effect shown when $N_p = 1$ and $\lambda_z = 0.023$. Thus, a better response could be reached with an online tuning of the weight factor that also allows to set a limit for voltage oscillations as described in [31] in addition with possibility of implementing variable saturation both in the generation of references and in its respective current control thanks to the decoupling map.

Similarly, using the oscilloscope, some relevant variables of the system are recorded and illustrated in Fig. 4.6 with a maneuver that includes three different speed operation. Thus, these show the currents frequency change both outside the converter and internally as consequence, the latter also having the external components in combination with the CMV frequency in the manner mentioned above and consistent with (3.3), while the amplitude of the cluster current at 800 rpm is significantly reduced compared to other speeds, requiring less intervention from the proposed energy control that would be reduced to a near-zero reference if the common-mode

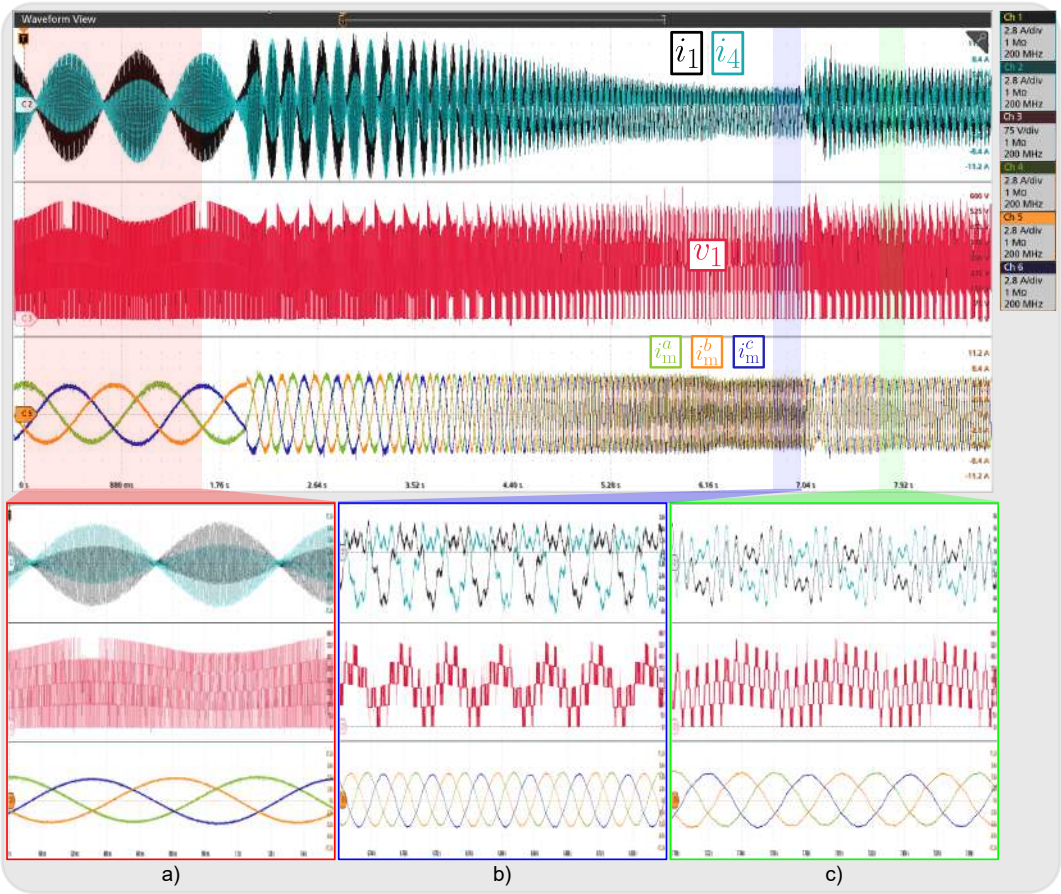

FIGURE 4.6: Experiment performance during start-up maneuver with load torque. Waveforms: i_1 (Ch 1), i_4 (Ch 2), v_1 (Ch 3), i_m^a (Ch 4), i_m^b (Ch 5), i_m^c (Ch 6) . (a) standstill (b) operating at 800 rpm ($\sim$ 27 Hz), and (c) operating at 400 rpm ($\sim$ 13 Hz)

voltage were omitted. On the other side, the currents of the induction machine do not vary significantly in amplitude after startup due to the imposed control saturation to achieve the previously mentioned slower dynamics. However, this contributes to increase voltage oscillations and, therefore, the circulating current reference.

4.1.2 Influence of the Extended Horizon in Steady-State

The influence of the prediction horizon will first be verified at a fixed operating point of 150 rpm ($\sim$ 5 Hz) with a constant load torque applied to the shaft. The operating point is chosen to demonstrate the performance at low speeds with a load that demands more control effort. The constraint in (3.23c) is considered as a box constraint, i.e., the upper and lower limits are set in a fixed value of 9 A.

Fig. 4.7 summarizes the experimental results in steady-state at 150 rpm, illustrating the trade-off between these performance indexes for several prediction horizons. Each point is obtained by adjusting the weighting factor λ_z to yield the same $\bar{I}_{cc}$ when the prediction horizon is increased from the step-one prediction case.

The first key point to highlight is the benefit of extending the prediction horizon in

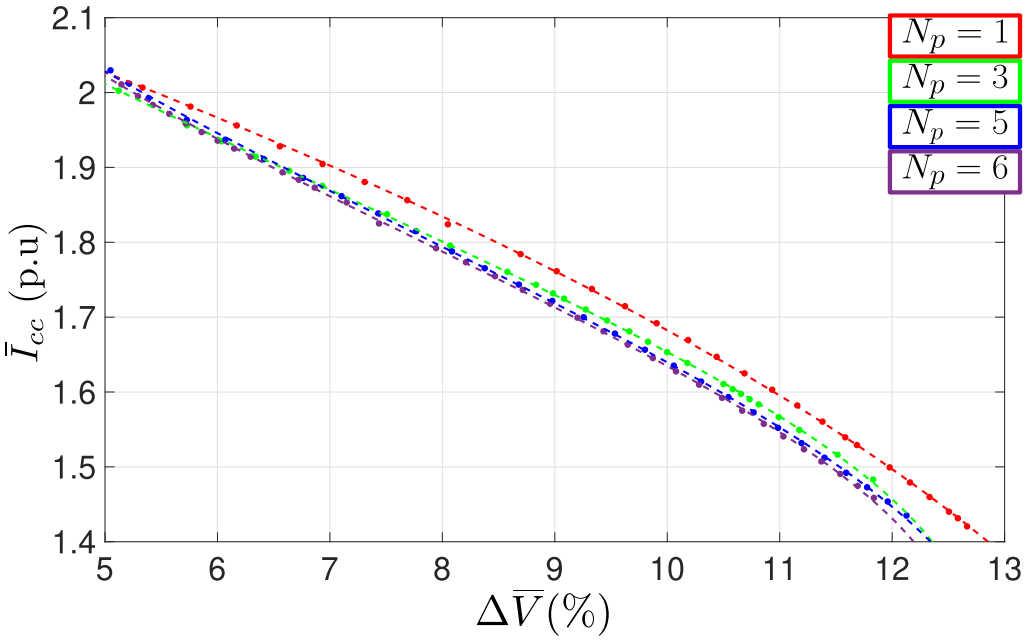

FIGURE 4.7: Experimental Result of the influence of Extended Prediction Horizon on Voltage Oscillations and the amount of Circulating Current required at constant speed $f = 5$ Hz.

the performance of an M2C-based drive. This extension reduces voltage oscillations while maintaining similar RMS values for the injected circulating current. Additionally, operating with a specific capacitor voltage deviation, the long-horizon approach reduces the RMS value of circulating currents, which would greatly enhance efficiency, particularly in higher-power drives. For instance, as shown in Fig. 4.7, if a capacitor voltage deviation of 10% is tolerable by the M2C, the RMS value of the circulating currents can be reduced by approximately 3%.

4.1.3 Proposed Algorithm performance

Given the proposed algorithm for solving the COCP, it is relevant to study the computational burden involved in using an extended horizon and its potential application to more advanced systems. Thus, Fig. 4.8 show the average iterations of the ADMM algorithm and the cost function of the COCP. The data considers the lowest choice of λ_z shown in Fig. 4.5, hence representing the situation with the highest computational requirement tested. Logically, the extension of the horizon implies an increase in iterations at each sampling time, with a doubling of iterations between the one-step horizon case and its counterpart with the maximum horizon chosen. Although the number of iterations does not exceed 12 when the longest horizon is applied, the convergence value tends toward the stopping criterion of the algorithm, which, if exceeded due to the effect of extending the horizon or reducing the weight factor, would result in unfeasibility in its implementation. This behavior is accentuated during the startup dynamics, which can be more demanding if a higher torque is allowed through the imposed current saturation, and therefore may cause the algorithm to operate improperly. In any case, the chosen criterion should be studied in greater detail according to the optimality achieved by the solution, with the first criterion of equation (2.13) being the appropriate indicator for

this, added to the implementation of an efficient solver for the subproblems that allows more iterations without exceeding the established criterion and thus, achieve an even longer horizon to provide a more optimal solution. The cost function given by (3.20a) increases due to the inclusion of new terms in the sum associated with the extended horizon. Also, this effect is amplified by the higher value of λ_z as the prediction horizon grows, which equally weights all the terms. This underscores the need for tuning the weight factors to adapt not only to the specific moment but also to the selected extended horizon.

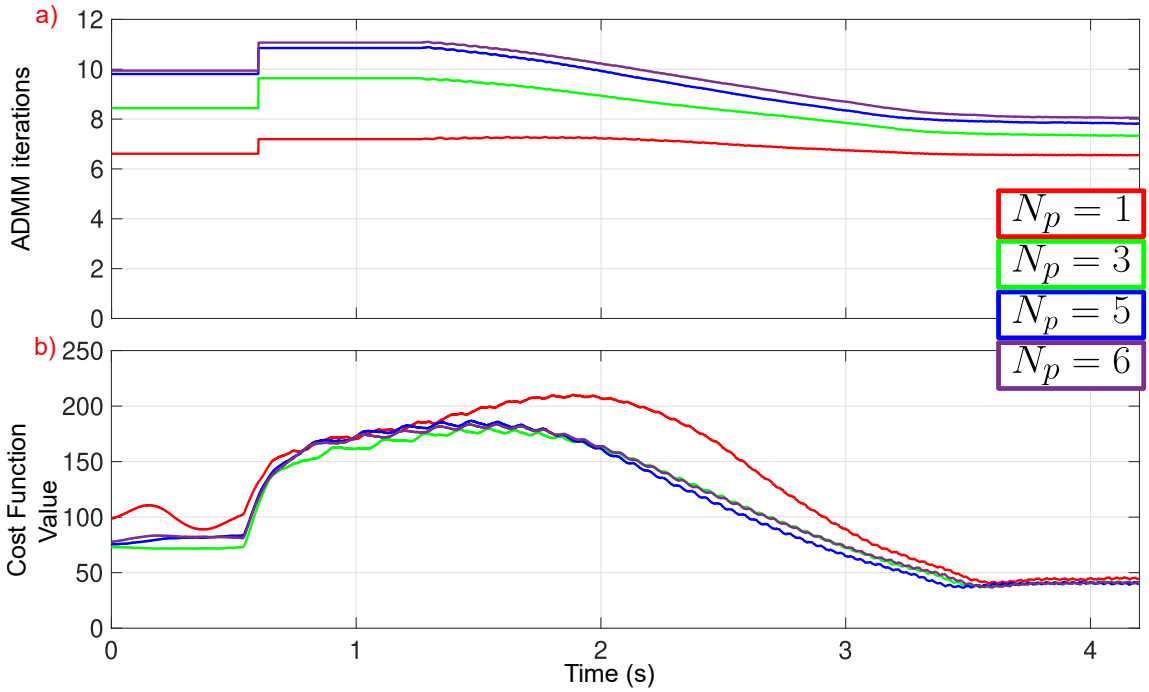

FIGURE 4.8: ADMM Algorithm performance during dynamic response with extended horizon through iterations on each sample time and cost function given by (3.20a).

It is also important to analyze the computational burden of this method in comparison to the conventional solution approach with an augmented matrix that considers all the κth terms from (3.25) and (3.26) for an immediate solution of the vectors $\boldsymbol{z}_\kappa$. In this regard, the calculation of the FLOPS necessary to solve the unconstrained problem in an extended horizon N_p will be considered, and is given by:

$$\boldsymbol{z}^{\text{uc}}(k) = -\mathbf{H}^{-1}(k)\mathbf{f}(k) \tag{4.4}$$

with

$$\begin{aligned} \mathbf{H}(k) &= \mathbf{B}(k)^T\mathbf{Q}\mathbf{B}(k) + \lambda_z\mathbf{I}_{6N_p} \\ \mathbf{f}(k) &= \mathbf{B}(k)^T\mathbf{Q}(\mathbf{E}_C(k) - \mathbf{E}_C^\star(k) + \mathbf{E}_{C0}(k)) \end{aligned} \tag{4.5}$$

Considering $\mathbf{B}, \mathbf{Q} \in \mathbb{R}^{6N_p}$ and $\mathbf{E}_C, \mathbf{E}_{C0}, \mathbf{E}_C^\star \in \mathbb{R}^{6N_p \times 1}$. On the other hand, the ADMM algorithm from (3.31) will also take the unconstrained solution in each subproblem, but the

TABLE 4.2: ADMM Algorithm Execution time.

Horizon	Max time (μs)
1	4,97
3	26,08
5	83,66
6	131,20

solution will depend on the iterations N_{it} performed until the convergence criterion is met. Thus, both algorithms will have the following total FLOPS:

$$\text{FLOPS}_{\text{Conv}} = 6N_p(120N_p^2 + 30N_p + 1) \tag{4.6}$$

$$\text{FLOPS}_{\text{ADMM}} = 2N_{it}(10N_p^3 + 56N_p^2 + 18N_p + 3) \tag{4.7}$$

The algorithms depend cubically on the chosen prediction horizon, and graphically, Fig. 4.9 shows how an increase in iterations implies that the algorithm proposed in this work becomes less efficient when N_p is low, necessitating an extended horizon to ensure that the ADMM method outperforms the conventional one. However, considering the results of Fig. 4.8, where on average no more than 12 iterations are required, the operation would lie between the green and blue curves in terms of the required FLOPS, making the ADMM method more suitable for the application and this is also reflected in its implementability. It should be noted that the analysis is conducted solely on the solution of the QP problem, as the other control tasks do not differ between methods.

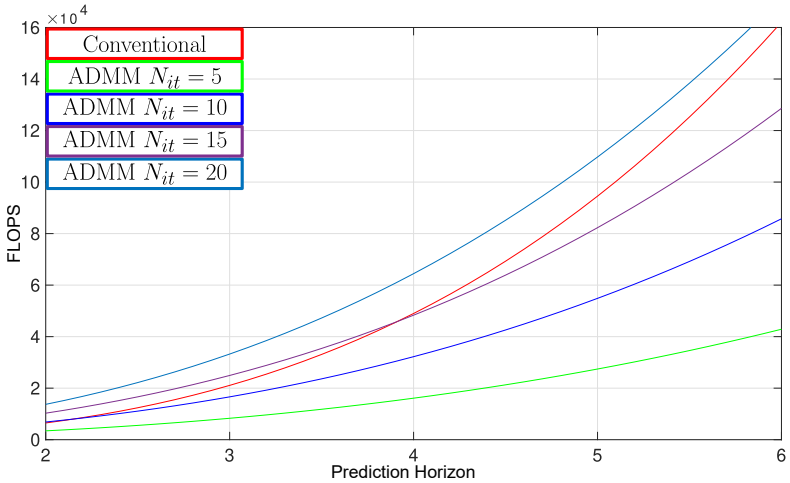

FIGURE 4.9: Total FLOPS for both Conventional and ADMM algorithm to performance ICB control.

Regarding execution time, Table 4.2 presents the maximum execution time during the most critical phase of operation, which corresponds to the point where the highest number of iterations is reached, as previously mentioned. The execution times increase cubically when considering a similar number of iterations, as observed in this case. For the maximum horizon, the algorithm utilizes 78% of the total computation time, thereby imposing a limit on the implementation for a higher N_p value with an equal or lower circulating current requirement.

5. Conclusions

The evolution and development of the grid as an increasingly complex system, where renewable energy generation, transmission via HVDC lines, and distribution through various applications such as EV-charger, storage systems and micro-grids are constantly demanding more quality and robustness from the power converters that link them with the entire grid. To meet these demands, the multilevel converter family has been introduced as a promising topology to achieve the objectives.

The massification of conventional two-level converters must be taken into account when discussing reliable features such as fault tolerance, scalability and harmonic suppression since these features were not inherently present without additional extensions. In this regard, the modular multilevel converter have an advantage by including and solving these recurring issues. However, an inherent challenge comes with these topologies due to the large increase in both passive and active components. As a result, the external control tasks must be carried out considering new internal tasks coming from the internal states such as managing internal states like energy/voltage and currents, which consequently implies a more sophisticated and complex control.

Furthermore, the external conditions can contribute to this challenge. For the M2C topology each capacitor voltage needs a proper and well-distributed balancing in addition to maintaining overall balance to provide sufficient energy for operation. This one-by-one energy balance becomes more difficult when converter output operates at low frequencies, representing a critical point that must be studied with increasingly advanced techniques, especially in a very common application like machine drives.

One of the aforementioned techniques is the presented and developed in this work which is based on a model predictive control that considers two general terms, which are contrasted by computing their squared norm error with a weight factor to emphasize one over the other. These two terms are the cluster energy vector and the circulating currents vector. The former denotes the balance task, while the currents act as the control effort in the optimization problem. Although the original model used is non-linear, the optimal solution is achieved by arbitrarilly

choosing one of the degrees of freedom, being in this work the common mode voltage which can not be a null variable in start-up drive applications. Therefore, the circulating currents remains as a control variable.

Then, the novelty of this control strategy lies in the algorithm used to solve the balance optimization problem. The alternating direction method of multipliers (ADMM) was applied whit its main feature being the decomposition of the problem into subproblems. Each subproblem considers the circulating currents of a single cluster as the variable to be optimized and the global solution is achieved by iterating until it satisfies a convergence criterion. In addition, this method was chosen to allow the incorporation of an extended horizon in a real implementation and to assess its performance.

To validate the hypothesis, a reduced experimental setup consisting of the M2C converter driving an induction machine was implemented, meanwhile the control algorithm was executed on an FPGA. Given the application, both stationary and transient behaviour were tested and assessed through an start-up and braking maneuvers considering a significant load torque. Then, indicators such as the standard deviation of voltage oscillations and the average RMS in circulating currents were stablished as KPIs to determine whether performance improvements were achieved.

Each test was carried out with a baseline case where the prediction horizon was limited to one step ahead, which was then compared with the same test but with an extended horizon. This was accompanied by an arbitrary tuning using the weight factor that penalizes control effort.

The steady-state results provided an initial insight into the effect of a longer horizon on performance. A significant improvement was observed at low speeds, with both indicators decreasing aforementioned, especially in more relaxed cases (i.e., where the circulating current demand is lower), while still maintaining the trade-off between more efficient operation and reduced voltage performance in terms of oscillations.

In this way, the previous results provide a basis for a comparison of the prediction horizons during a dynamic maneuver. For each chosen horizon, a fixed tuning of the weight factor was set to ensure a similar or lower demand for circulating currents.

The transient behaviour confirmed the proposed approach, achieving greater efficiency and reducing voltage oscillations with the iterative proposed ADMM algorithm, which provided optimal results with few iterations per sampling time, even with a long horizon and under the most critical operating point (low-speed high-torque). Furthermore, the constrained optimal control problem was solved while keeeping the constraint on currents active to prevent overmodulation and damages. It is worth noting that the common mode voltage, as an arbitrary signal, sometimes had an undesired impact because its implementation was not co-optimized with the currents, leading to deviations in the capacitor voltages.

Although the current implementation achieved long prediction horizons, an evaluation of the ADMM algorithm showed a considerable increase in execution time, consuming more than a half of the computation time when the maximum achievable horizon was selected. Nevertheless, the results support the algorithm over conventional method which cannot be implemented. Moreover, the ADMM algorithm can be further improved by employing more efficient solvers for the subproblems, allowing for an even longer prediction horizon.

Looking forward, several aspects should be considered for future work. These include the implementation of real-time tuning of the weight factor, which would allow for the definition of performance objectives throughout the startup process. This is particularly important given

the impact of the weight factor as a balancing parameter between efficiency and oscillation reduction. Additionally, the possibility of making smooth transitions between low- and high-frequency operations—where the injection of common mode voltage can be omitted for better use of the modulated voltage—should be explored. On the other hand, there is the treatment of the optimization problem together with a strategy that allows for the co-optimization of both degrees of freedom (circulating currents and common mode voltage). This would lead to more robust control and prevent issues such as overmodulation or the arbitrary selection of signals that, in some cases, are not suitable.

Bibliography

[1] F. A. Rubio Achondo, "Control predictivo basado en secuencia de conmutación óptima para un conversor de tres puertos aplicado a vehículos eléctricos," Master's thesis, Pontificia Universidad Catolica de Chile, 2024.

[2] Andrés Mora Castro, "Apuntes para la asignatura Accionamientos Eléctricos," 2021.

[3] D. E. Knuth, *The Art of Computer Programming*, vol. 1-4. Reading, Massachusetts: Addison-Wesley, 3rd ed., 1997.

[4] R. Singh, P. Paniyil, and Z. Zhang, "Transformative role of power electronics: In solving climate emergency," *IEEE Power Electronics Magazine*, vol. 9, no. 2, pp. 39–47, 2022.

[5] S. Kouro, J. I. Leon, D. Vinnikov, and L. G. Franquelo, "Grid-connected photovoltaic systems: An overview of recent research and emerging pv converter technology," *IEEE Industrial Electronics Magazine*, vol. 9, no. 1, pp. 47–61, 2015.

[6] A. Shourangiz-Haghighi, M. Diazd, Y. Zhang, J. Li, Y. Yuan, R. Faraji, L. Ding, and J. M. Guerrero, "Developing more efficient wind turbines: A survey of control challenges and opportunities," *IEEE Industrial Electronics Magazine*, vol. 14, no. 4, pp. 53–64, 2020.

[7] K. Friedrich, "Modern hvdc plus application of vsc in modular multilevel converter topology," in *2010 IEEE International Symposium on Industrial Electronics*, pp. 3807–3810, 2010.

[8] Q. Peng, Q. Jiang, Y. Yang, T. Liu, H. Wang, and F. Blaabjerg, "On the stability of power electronics-dominated systems: Challenges and potential solutions," *IEEE Transactions on Industry Applications*, vol. 55, no. 6, pp. 7657–7670, 2019.

[9] F. Blaabjerg, Y. Yang, K. Ma, and X. Wang, "Power electronics-the key technology for renewable energy system integration," *2015 International Conference on Renewable Energy Research and Applications, ICRERA 2015*, pp. 1618–1626, 2015.

[10] M. Diaz, R. Cárdenas Dobson, E. Ibaceta, A. Mora, M. Urrutia, M. Espinoza, F. Rojas, and P. Wheeler, "An overview of applications of the modular multilevel matrix converter," *Energies*, vol. 13, no. 21, 2020.

[11] M. A. Perez, S. Bernet, J. Rodriguez, S. Kouro, and R. Lizana, "Circuit topologies, modeling, control schemes, and applications of modular multilevel converters," *IEEE Transactions on Power Electronics*, vol. 30, pp. 4–17, Jan 2015.

[12] S. Kouro, M. Malinowski, K. Gopakumar, J. Pou, L. G. Franquelo, B. Wu, J. Rodriguez, M. A. Perez, and J. I. Leon, "Recent advances and industrial applications of multilevel converters," *IEEE Transactions on Industrial Electronics*, vol. 57, pp. 2553–2580, Aug 2010.

[13] H. Akagi, "Classification, terminology, and application of the modular multilevel cascade converter (mmcc)," *IEEE Transactions on Power Electronics*, vol. 26, pp. 3119–3130, Nov 2011.

[14] A. Dekka, B. Wu, V. Yaramasu, R. L. Fuentes, and N. R. Zargari, "Model predictive control of high-power modular multilevel converters, an overview," *IEEE Journal of Emerging and Selected Topics in Power Electronics*, pp. 1–1, 2018.

[15] M. A. Perez, S. Ceballos, G. Konstantinou, J. Pou, and R. P. Aguilera, "Modular Multilevel Converters: Recent Achievements and Challenges," *IEEE Open Journal of the Industrial Electronics Society*, vol. 2, pp. 224–239, 2021.

[16] P. Bravo, J. Pereda, M. M. C. Merlin, S. Neira, T. Green, and F. Rojas, "Modular multilevel matrix converter as solid state transformer for medium and high voltage substations," *IEEE Transactions on Power Delivery*, pp. 1–1, 2022.

[17] M. A. Perez, S. Bernet, J. Rodriguez, S. Kouro, and R. Lizana, "Circuit topologies, modeling, control schemes, and applications of modular multilevel converters," *IEEE Transactions on Power Electronics*, vol. 30, no. 1, pp. 4–17, 2015.

[18] F. Briz, M. Lopez, A. Rodriguez, and M. Arias, "Modular power electronic transformers: Modular multilevel converter versus cascaded h-bridge solutions," *IEEE Industrial Electronics Magazine*, vol. 10, no. 4, pp. 6–19, 2016.

[19] M. Al-Tameemi, Y. Miura, J. Liu, H. Bevrani, and T. Ise, "A Novel Control Scheme for Multi-Terminal Low-Frequency AC Electrical Energy Transmission Systems Using Modular Multilevel Matrix Converters and Virtual Synchronous Generator Concept," *Energies*, vol. 13, p. 747, feb 2020.

[20] M. Diaz, R. Cardenas, M. Espinoza, F. Rojas, A. Mora, J. C. Clare, and P. Wheeler, "Control of wind energy conversion systems based on the modular multilevel matrix converter," *IEEE Transactions on Industrial Electronics*, vol. 64, no. 11, pp. 8799–8810, 2017.

[21] W. Kawamura, M. Hagiwara, and H. Akagi, "Control and experiment of a modular multilevel cascade converter based on triple-star bridge cells," *IEEE Transactions on Industry Applications*, vol. 50, no. 5, pp. 3536–3548, 2014.

[22] R. Lizana, M. A. Perez, S. Bernet, J. R. Espinoza, and J. Rodriguez, "Control of arm capacitor voltages in modular multilevel converters," *IEEE Transactions on Power Electronics*, vol. 31, pp. 1774–1784, Feb 2016.

[23] M. Espinoza-B, R. Cárdenas, J. Clare, D. Soto-Sanchez, M. Diaz, E. Espina, and C. M. Hackl, "An integrated converter and machine control system for mmc-based high-power drives," *IEEE Transactions on Industrial Electronics*, vol. 66, no. 3, pp. 2343–2354, 2019.

[24] D. Karwatzki and A. Mertens, "Generalized control approach for a class of modular multilevel converter topologies," *IEEE Transactions on Power Electronics*, vol. 33, pp. 2888–2900, April 2018.

[25] Y. Arias-Esquivel, R. Cárdenas, L. Tarisciotti, M. Díaz, and A. Mora, "A two-step continuous-control-set mpc for modular multilevel converters operating with variable output voltage and frequency," *IEEE Transactions on Power Electronics*, pp. 1–12, 2023.

[26] W. Kawamura, K. Chen, M. Hagiwara, and H. Akagi, "A low-speed, high-torque motor drive using a modular multilevel cascade converter based on triple-star bridge cells (mmcc-tsbc)," *IEEE Transactions on Industry Applications*, vol. 51, pp. 3965–3974, Sep. 2015.

[27] S. Vazquez, J. Rodriguez, M. Rivera, L. G. Franquelo, and M. Norambuena, "Model predictive control for power converters and drives: Advances and trends," *IEEE Transactions on Industrial Electronics*, vol. 64, pp. 935–947, Feb 2017.

[28] F. Donoso, A. Mora, R. Cardenas, A. Angulo, D. Saez, and M. Rivera, "Finite-set model-predictive control strategies for a 3l-npc inverter operating with fixed switching frequency," *IEEE Transactions on Industrial Electronics*, vol. 65, pp. 3954–3965, May 2018.

[29] R. Baidya, R. P. Aguilera, P. Acuna, S. Vazquez, and H. d. T. Mouton, "Multistep model predictive control for cascaded h-bridge inverters: Formulation and analysis," *IEEE Transactions on Power Electronics*, vol. 33, pp. 876–886, Jan 2018.

[30] P. Karamanakos and T. Geyer, "Guidelines for the design of finite control set model predictive controllers," *IEEE Transactions on Power Electronics*, vol. 35, no. 7, pp. 7434–7450, 2020.

[31] Y. Arias-Esquivel, R. Cárdenas, M. Urrutia, M. Diaz, L. Tarisciotti, and J. C. Clare, "Continuous control set model predictive control of a modular multilevel converter for drive applications," *IEEE Transactions on Industrial Electronics*, vol. 70, no. 9, pp. 8723–8733, 2023.

[32] R. Fletcher, "A General Quadratic Programming Algorithm," *IMA Journal of Applied Mathematics*, vol. 7, pp. 76–91, 02 1971.

[33] H. J. Ferreau, H. G. Bock, and M. Diehl, "An online active set strategy to overcome the limitations of explicit mpc," *International Journal of Robust and Nonlinear Control*, vol. 18, no. 8, pp. 816–830, 2008.

[34] N. Karmarkar, "A new polynomial-time algorithm for linear programming," *Combinatorica*, no. 4, p. 373–395, 1984.

[35] A. Domahidi, A. U. Zgraggen, M. N. Zeilinger, M. Morari, and C. N. Jones, "Efficient interior point methods for multistage problems arising in receding horizon control," in *2012 IEEE 51st IEEE Conference on Decision and Control (CDC)*, pp. 668–674, 2012.

[36] Y. Nesterov, "A method for solving the convex programming problem with convergence rate $o(1/k^2)$," *Proceedings of the USSR Academy of Sciences*, vol. 269, pp. 543–547, 1983.

[37] E. Klintberg and S. Gros, "Approximate inverses in preconditioned fast dual gradient methods for mpc," *IFAC-PapersOnLine*, vol. 50, no. 1, pp. 5901–5906, 2017. 20th IFAC World Congress.

[38] S. Boyd, N. Parikh, E. Chu, B. Peleato, and J. Eckstein, *Distributed Optimization and Statistical Learning via the Alternating Direction Method of Multipliers*. 2011.

[39] J. Escárate, R. López, A. L. Cedeño, J. C. Agüero, C. Silva, and G. Carvajal, "Fpga implementation of admm for model predictive control in a dc/ac converter," in *2022 IEEE International Conference on Automation/XXV Congress of the Chilean Association of Automatic Control (ICA-ACCA)*, pp. 1–6, 2022.

[40] SIEMENS, "HVDC PLUS," https://www.siemens-energy.com/global/en/offerings/power-transmission/portfolio/high-voltage-direct-current-transmission-solutions/hvdc-plus.html.

[41] Benshaw, "Medium voltage Variable Frequency Drive M2L 3000 Series," https://benshaw.com/wp-content/uploads/2020/01/benshaw-m2l-3000-brochure.pdf.

[42] SIEMENS, "SINAMICS Perfect Harmonic GH150 and SH150," https://new.siemens.com/global/en/products/drives/sinamics/ medium-voltage-converters.html.

[43] SIEMENS, "Innomotics Medium Voltage Drives," https://www.innomotics.com/hub/en/portfolio/products/m voltage-drives.

[44] F. Ma, Q. Xu, Z. He, C. Tu, Z. Shuai, A. Luo, and Y. Li, "A railway traction power conditioner using modular multilevel converter and its control strategy for high-speed railway system," *IEEE Transactions on Transportation Electrification*, vol. 2, no. 1, pp. 96–109, 2016.

[45] M. Lei, Y. Li, Z. Li, C. Zhao, F. Xu, F. Gao, and P. Wang, "A single-phase five-branch direct ac-ac modular multilevel converter for railway power conditioning," *IEEE Transactions on Industrial Electronics*, vol. 67, pp. 4292–4304, June 2020.

[46] N. Thitichaiworakorn, M. Hagiwara, and H. Akagi, "A medium-voltage large wind turbine generation system using an ac/ac modular multilevel cascade converter," *IEEE Journal of Emerging and Selected Topics in Power Electronics*, vol. 4, pp. 534–546, June 2016.

[47] J. Holtz, "The representation of ac machine dynamics by complex signal flow graphs," *IEEE Transactions on Industrial Electronics*, vol. 42, pp. 263–271, June 1995.

[48] M. Malinowski, M. P. Kazmierkowski, and A. M. Trzynadlowski, "A comparative study of control techniques for pwm rectifiers in ac adjustable speed drives," *IEEE Transactions on Power Electronics*, vol. 18, pp. 1390–1396, Nov 2003.

[49] M. Espinoza, R. Cárdenas, M. Díaz, and J. C. Clare, "An enhanced *dq*-based vector control system for modular multilevel converters feeding variable-speed drives," *IEEE Transactions on Industrial Electronics*, vol. 64, no. 4, pp. 2620–2630, 2017.

[50] M. Diaz, R. Cardenas, M. Espinoza, C. M. Hackl, F. Rojas, J. C. Clare, and P. Wheeler, "Vector control of a modular multilevel matrix converter operating in the full output-frequency range," *IEEE Transactions on Industrial Electronics*, pp. 1–1, 2018.

[51] W. Kawamura, M. Hagiwara, and H. Akagi, "Control and experiment of a modular multilevel cascade converter based on triple-star bridge cells," *IEEE Transactions on Industry Applications*, vol. 50, pp. 3536–3548, Sep. 2014.

[52] M. Diaz, R. Cardenas, M. Espinoza, F. Rojas, A. Mora, J. C. Clare, and P. Wheeler, "Control of wind energy conversion systems based on the modular multilevel matrix converter," *IEEE Transactions on Industrial Electronics*, vol. 64, pp. 8799–8810, Nov 2017.

[53] B. Fan, K. Wang, Z. Zheng, L. Xu, and Y. Li, "Optimized branch current control of modular multilevel matrix converters under branch fault conditions," *IEEE Transactions on Power Electronics*, vol. 33, no. 6, pp. 4578–4583, 2018.

[54] B. Fan, K. Wang, P. Wheeler, C. Gu, and Y. Li, "An optimal full frequency control strategy for the modular multilevel matrix converter based on predictive control," *IEEE Transactions on Power Electronics*, vol. 33, pp. 6608–6621, Aug 2018.

[55] M. Hagiwara and H. Akagi, "Control and experiment of pulsewidth-modulated modular multilevel converters," *IEEE Transactions on Power Electronics*, vol. 24, no. 7, pp. 1737–1746, 2009.

[56] H. Akagi, "Multilevel converters: Fundamental circuits and systems," *Proceedings of the IEEE*, vol. 105, no. 11, pp. 2048–2065, 2017.

[57] M. Urrutia, A. Mora, A. Angulo, P. Lezana, R. Cardenas, and M. Diaz, "A novel capacitor voltage balancing strategy for modular multilevel converters," in *2017 IEEE Southern Power Electronics Conference (SPEC)*, pp. 1–6, Dec 2017.

[58] A. Mora, M. Urrutia, R. Cárdenas, A. Angulo, M. Espinoza, M. Díaz, and P. Lezana, "Model-predictive-control-based capacitor voltage balancing strategies for modular multilevel converters," *IEEE Transactions on Industrial Electronics*, vol. 66, pp. 2432–2443, March 2019.

[59] W. van der Merwe, "Natural balancing of the 2-cell modular multilevel converter," *IEEE Transactions on Industry Applications*, vol. 50, no. 6, pp. 4028–4035, 2014.

[60] G. Konstantinou, J. Pou, S. Ceballos, R. Darus, and V. G. Agelidis, "Switching frequency analysis of staircase-modulated modular multilevel converters and equivalent pwm techniques," *IEEE Transactions on Power Delivery*, vol. 31, no. 1, pp. 28–36, 2016.

[61] J. I. Leon, S. Kouro, L. G. Franquelo, J. Rodríguez, and B. Wu, "The Essential Role and the Continuous Evolution of Modulation Techniques for Voltage-Source Inverters in the Past, Present, and Future Power Electronics," *Dielectrics and Electrical Insulation, IEEE Transactions on*, vol. 63, no. 5, pp. 2688–2701, 2016.

[62] J. Mei, K. Shen, B. Xiao, L. M. Tolbert, and J. Zheng, "A new selective loop bias mapping phase disposition pwm with dynamic voltage balance capability for modular multilevel converter," *IEEE Transactions on Industrial Electronics*, vol. 61, no. 2, pp. 798–807, 2014.

[63] X. Shi, Z. Wang, L. M. Tolbert, and F. Wang, "A comparison of phase disposition and phase shift pwm strategies for modular multilevel converters," in *2013 IEEE Energy Conversion Congress and Exposition*, pp. 4089–4096, 2013.

[64] J. I. Leon, S. Vazquez, and L. G. Franquelo, "Multilevel converters: Control and modulation techniques for their operation and industrial applications," *Proceedings of the IEEE*, vol. 105, no. 11, pp. 2066–2081, 2017.

[65] E. Chatzinikolaou and D. J. Rogers, "Hierarchical distributed balancing control for large-scale reconfigurable ac battery packs," *IEEE Transactions on Power Electronics*, vol. 33, no. 7, pp. 5592–5602, 2018.

[66] F. Kammerer, J. Kolb, and M. Braun, "Fully decoupled current control and energy balancing of the modular multilevel matrix converter," in *2012 15th International Power Electronics and Motion Control Conference (EPE/PEMC)*, pp. LS2a.3–1–LS2a.3–8, 2012.

[67] J. Kolb, F. Kammerer, M. Gommeringer, and M. Braun, "Cascaded control system of the modular multilevel converter for feeding variable-speed drives," *IEEE Transactions on Power Electronics*, vol. 30, no. 1, pp. 349–357, 2015.

[68] T. Geyer, G. Papafotiou, and M. Morari, "Model predictive direct torque control part i: Concept, algorithm, and analysis," *IEEE Transactions on Industrial Electronics*, vol. 56, pp. 1894–1905, June 2009.

[69] D. E. Quevedo, R. P. Aguilera, and T. Geyer, *Predictive Control in Power Electronics and Drives: Basic Concepts, Theory, and Methods.* Springer International Publishing, 2014.

[70] A. Linder and R. Kennel, "Direct model predictive control - a new direct predictive control strategy for electrical drives," in *2005 European Conference on Power Electronics and Applications*, pp. 10 pp.–P.10, Sept 2005.

[71] R. Baños, F. Manzano-Agugliaro, F. Montoya, C. Gil, A. Alcayde, and J. Gómez, "Optimization methods applied to renewable and sustainable energy: A review," *Renewable and Sustainable Energy Reviews*, vol. 15, no. 4, pp. 1753–1766, 2011.

[72] R. Baños, F. Manzano-Agugliaro, F. Montoya, C. Gil, A. Alcayde, and J. Gómez, "Optimization methods applied to renewable and sustainable energy: A review," *Renewable and Sustainable Energy Reviews*, vol. 15, no. 4, pp. 1753–1766, 2011.

[73] J. Nocedal and S. J. Wright, *Numerical Optimization.* 2 ed., 2006.

[74] D. M. Manfred Gilli and E. Schumann, *Numerical Methods and Optimization in Finance (Second Edition)*. Academic Press, 2019.

[75] D. Han and X. Yuan, "A note on the alternating direction method of multipliers," *Journal of Optimization Theory and Applications*, vol. 155, no. 2, pp. 1573–2878, 2012.

[76] D. P. Bertsekas, "Extended monotropic programming and duality," *Journal of Optimization Theory and Applications*, vol. 139, no. 2, pp. 1573–2878, 2008.

[77] W. Deng and W. Yin, "On the global and linear convergence of the generalized alternating direction method of multipliers," *Journal of Scientific Computing*, vol. 66, p. 889–916, 2016.

[78] W. Deng, M.-J. Lai, Z. Peng, and W. Yin, "Parallel multi-block admm with $o(1/k)$ convergence," *Journal of Scientific Computing*, vol. 71, pp. 1573–7691, 2017.

[79] Y. Zhang, E. Dall'Anese, and M. Hong, "Online proximal-admm for time-varying constrained convex optimization," *IEEE Transactions on Signal and Information Processing over Networks*, vol. 7, pp. 144–155, 2021.

[80] R. Cuzmar, A. Montenegro, A. Mora, J. Pereda, and R. P. Aguilera, "Constrained mpc for intercluster energy control of modular multilevel matrix converters," *IEEE Transactions on Industrial Electronics*, pp. 1–11, 2023.

[81] J. Rodriguez, C. Garcia, A. Mora, F. Flores-Bahamonde, P. Acuna, M. Novak, Y. Zhang, L. Tarisciotti, S. A. Davari, Z. Zhang, F. Wang, M. Norambuena, T. Dragicevic, F. Blaabjerg, T. Geyer, R. Kennel, D. A. Khaburi, M. Abdelrahem, Z. Zhang, N. Mijatovic, and R. P. Aguilera, "Latest advances of model predictive control in electrical drives part i: Basic concepts and advanced strategies," *IEEE Transactions on Power Electronics*, vol. 37, no. 4, pp. 3927–3942, 2022.

[82] U. Maeder and M. Morari, "Offset-free reference tracking with model predictive control," *Automatica*, vol. 46, no. 9, pp. 1469–1476, 2010.

[83] M. Espinoza, M. Diaz, F. Donoso, A. Letelier, and R. Cardenas, "Control and operation of the mmc-based drive with reduced capacitor voltage fluctuations," *The Journal of Engineering*, vol. 2019, 04 2019.

[84] S. Boyd, N. Parikh, E. Chu, B. Peleato, and J. Eckstein, "Distributed optimization and statistical learning via the alternating direction method of multipliers," *Foundations and Trends in Machine Learning*, vol. 3, no. 1, pp. 1–122, 2010.

[85] X. Wang, M. Hong, S. Ma, and Z.-Q. Luo, "Solving multiple-block separable convex minimization problems using two-block alternating direction method of multipliers," 2013.

[86] D. P. Bertsekas, *Nonlinear Programming*. 2016.